Defence Research and Development Canada
Recherche et développement pour la défense Canada

DRDC | RDDC

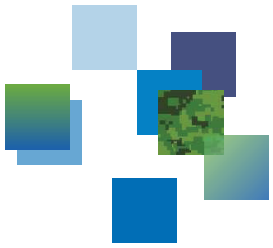

Study of Compressive Sensing for Tomographic Processing in Satellite (SAR) Systems

David Kirkland
DRDC – Ottawa Research Centre

Defence Research and Development Canada

Scientific Report
DRDC-RDDC-2016-R173
September 2016

Canada

Study of Compressive Sensing for Tomographic Processing in Satellite (SAR) Systems

David Kirkland
DRDC – Ottawa Research Centre

Defence Research and Development Canada
Scientific Report
DRDC-RDDC-2016-R173
September 2016

Abstract

Tomographic processing involves coherent processing of multiple passes of Synthetic Aperture Radar (SAR) imagery to provide elevation discrimination in a SAR range/azimuth pixel. This report investigates the use of C-band satellites such as RADARSAT-2 or the RADARSAT Constellation Mission (RCM) for tomographic processing. This report uses a Compressive Sensing (CS) approach to accomplish the tomographic processing. Four different satellite geometries are simulated to provide a range of operating environments. For each of the geometries the performance against single target and two target scenarios is measured at various Signal to Noise ratios (SNRs) using simulated data. This report also includes theoretical analysis on the resolution and the Cramer-Rao Lower Bounds (CRLB) on the deviation of elevation estimates.

Significance for defence and security

Tomographic processing utilizes multiple coherent collections of Synthetic Aperture Radar (SAR) data imagery to provide elevation resolution within a SAR resolution cell. This elevation discrimination results in increased situational awareness of the observed area. This report examines the use of Compressive Sensing (CS) techniques for tomographic processing and gives an indication of the likely performance achievable with systems like RADARSAT-2 or the RADARSAT Constellation Mission (RCM). The results in this report indicate that the applicability of CS techniques for tomographic will be limited to persistent targets with a high coherence and high signal to noise ratio.

Résumé

Le traitement tomographique fait appel au traitement cohérent de l'imagerie de radar à synthèse d'ouverture (RSO) pour établir la discrimination des altitudes topographiques dans un pixel distance/azimut. Ce rapport examine l'utilisation des satellites en bande C, comme RADARSAT-2, ou ceux relevant de la mission de la Constellation RADARSAT (MCR) pour le traitement tomographique. Ce rapport utilise une méthode d'acquisition comprimée pour accomplir le traitement tomographique. Quatre géométries de satellites différentes sont simulées pour fournir une gamme d'environnements d'exploitation. Pour chacune des géométries, on a mesuré le rendement en fonction de scénarios à cible unique et à deux cibles à divers rapports signal/bruit (rapports S/B) à partir de données simulées. Ce rapport comprend également une analyse théorique de la résolution et des limites inférieures de Cramer-Rao s'appliquant à l'écart entre estimations d'altitude.

Importance pour la défense et la sécurité

Le traitement tomographique fait appel au traitement cohérent de l'imagerie de radar à synthèse d'ouverture (RSO) pour établir la discrimination des altitudes topographiques dans un pixel distance/azimut. Ce rapport examine l'utilisation des satellites en bande C, comme RADARSAT-2, ou ceux relevant de la mission de la Constellation RADARSAT (MCR) pour le traitement tomographique. Ce rapport utilise une méthode d'acquisition comprimée pour accomplir le traitement tomographique. Quatre géométries de satellites différentes sont simulées pour fournir une gamme d'environnements d'exploitation. Pour chacune des géométries, on a mesuré le rendement en fonction de scénarios à cible unique et à deux cibles à divers rapports signal/bruit (rapports S/B) à partir de données simulées. Ce rapport comprend également une analyse théorique de la résolution et des limites inférieures de Cramer-Rao s'appliquant à l'écart entre estimations d'altitude.

Table of contents

List of figures

List of tables

1 Introduction

Interferometric Synthetic Aperture Radar (InSAR) is a family of techniques which examine the phase information between two or more coherent Synthetic Aperture Radar (SAR) images to extract additional information beyond the reflectivity of the scene scatterers. Utilizing the phase information in a pair of repeat-pass coherent SAR images interferometry can determine the scatterer elevation. A good review of interferometry is provided in [1, 2]. Additional data collection passes allow time varying changes in elevation to be measured. InSAR implicitly assumes the presence of only a single scatterer in each SAR resolution cell.

SAR Tomography is an extension of InSAR for analysis of multiple coherent data collections; providing discrimination of multiple scatterers in the elevation dimension within a SAR resolution cell. Tomography goes beyond analyzing the phase difference between successive SAR images and attempts to model the elevation components within the SAR resolution cell. The repeat passes can be used to create a synthetic aperture in the elevation direction and separate targets in elevation. Tomography can also be extended to measure the time varying changes in elevation of the targets as well [3].

Simulations in this report utilize the technical operating parameters of RADARSAT-2 (pulse bandwidth and frequency) as a basis for measuring the achievable tomographic performance of RADARSAT-2 and other similar satellite systems such as the RADARSAT Constellation Mission (RCM). Section 2 describes the tomographic problem. Section 3 provides a brief overview of Compressive Sensing (CS) issues and formulations. Section 4 provides a theoretical analysis of the tomographic problem, including the resolution and Cramer-Rao bounds, and also presents the simulation results.

1.1 Mathematical notation

The following notation conventions are used throughout this report. Vectors are denoted by lowercase bold variables and matrices are denoted by uppercase bold variables. Given a vector $\boldsymbol{x}$, the l_2 norm of the is given as:

$$\|\boldsymbol{x}\|_2 = \sqrt{\sum_i |x_i|^2}, \tag{1}$$

where x_i denotes the ith component of the vector $\boldsymbol{x}$. The l_1 norm of the vector $\boldsymbol{x}$ is given as:

$$\|\boldsymbol{x}\|_1 = \sum_i |x_i| . \tag{2}$$

The l_0 norm of the vector $\boldsymbol{x}$ is given as:

$$\|\boldsymbol{x}\|_0 = \sum_i I(x_i), \tag{3}$$

where the function $I()$ is defined as:

$$I(x_i) = \begin{cases} 0 & \text{if } x_i = 0 \\ 1 & \text{otherwise} \end{cases} \tag{4}$$

The l_0 norm is simply the number of non-zero elements in the vector. The l_0 norm is actually a pseudo norm because it is does not satisfy homogeneity property of norms, i.e., $\|\alpha\boldsymbol{x}\|_0 \neq |\alpha| \|\boldsymbol{x}\|_0$, where α is a scalar.

Given a matrix $\boldsymbol{A}$, the Frobenius norm is given as:

$$\|\boldsymbol{A}\|_F = \sqrt{\sum_i \sum_j |a_{ij}|^2}, \tag{5}$$

where a_{ij} is the element of $\boldsymbol{A}$ in the ith row and jth column.

2 Tomography

Consider the multi-pass satellite SAR geometry shown in Figure 1. The satellite passes through N different orbits. The u axis is taken perpendicular to the line of sight. The position of each satellite pass is given by u_n, $n = 1, \ldots, N$ and the satellite velocity is perpendicular to the plane of the figure. For now it is assumed that the repeat passes fall exactly on the u axis. This assumption simplifies the current analysis and will be relaxed later on. After the SAR images have been formed by range and azimuth compression the set of measurements at each pixel are used to resolve vertical detail. Some SAR resolution cells will not contain any vertical detail due to the lack of any scatterer structure, while other resolution cells may have vertical detail when volumetric or composite scatterers are present. The length of the perpendicular baseline $L_\perp$ is given by $|u_N - u_1|$. The s axis is defined such that any scatterers located along this axis will appear at the same range-azimuth cell of the SAR image. In reality the s axis will be a curve but due to the large orbital altitude of the satellites it is well approximated by a straight line that is perpendicular to the line of sight.

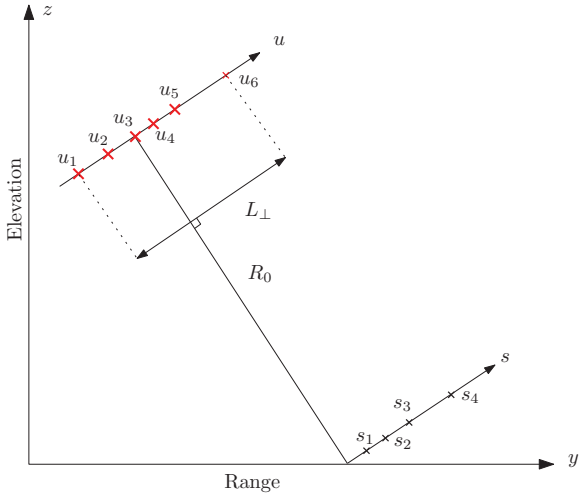

Figure 1: *Idealized tomography geometry.*

The range between the radar at position u and the range/elevation point s is given by:

$$R(u) = \sqrt{R_0^2 + (u - s)^2}, \tag{6}$$

where R_0 is the slant range from the centre of the array to the ground. Since u and s

will be small in comparison to R_0, the previous expression can be approximated by:

$$\begin{aligned} R(u) &= \sqrt{R_0^2+u^2}\sqrt{1-\frac{2us-s^2}{R_0^2+u^2}} \\ &\approx \sqrt{R_0^2+u^2}\left(1-\frac{us}{R_0^2+u^2}\right) \\ &\approx \sqrt{R_0^2+u^2}-\frac{us}{R_0}. \end{aligned} \tag{7}$$

The full derivation of (7) is given in Annex A. The corresponding two-way phase delay associated with this range is:

$$\begin{aligned} \phi(u) &= -\frac{4\pi}{\lambda}\left[\sqrt{R_0^2+u^2}-\frac{us}{R_0}\right] \\ &= -2k\left[\sqrt{R_0^2+u^2}-\frac{us}{R_0}\right], \end{aligned} \tag{8}$$

where λ is the radar operating wavelength and $k = 2\pi/\lambda$ is the corresponding wave number. We denote the reference range as $R_{ref}(u) = \sqrt{R_0^2+u^2}$. The corresponding phase response is given by $\phi_{ref}(u) = -2kR_{ref}(u)$. This type of reference range is commonly used in Spotlight SAR signal processing and the removal of this reference range is referred to as deramping [4]. The phase after the removal of the phase due the reference range is given by:

$$\begin{aligned} \triangle\phi(u) &= \phi(u)-\phi_{ref}(u) \\ &= -2k\left[\sqrt{R_0^2+u^2}-\frac{us}{R_0}\right]+2k\sqrt{R_0^2+u^2} \\ &= 2k\frac{us}{R_0}. \end{aligned} \tag{9}$$

Let g_n denote the signal in a fixed azimuth and range pixel of the nth satellite pass after removal of the phase due to the reference range.Then g_n consists of contributions from scatters located at located along the s axis and is given by:

$$g_n = \int \gamma(s)e^{j2k\frac{u_n s}{R_0}}ds, \tag{10}$$

where $\gamma(s)$ represents the scattering strength along the s axis. We can write the received signal for all the satellite passes in vector format by letting $\mathbf{g} = [g_1,\, g_2,\, \ldots,\, g_N]^T$. By sampling at points $s_q\,(q = 1, \ldots, Q)$ along the s axis we can form a discrete model Then we have:

$$\begin{aligned} \mathbf{g} &= [\mathbf{a}(s_1),\, \mathbf{a}(s_2), \ldots, \mathbf{a}(s_Q)]\boldsymbol{\gamma} \\ &= \mathbf{A}\boldsymbol{\gamma}, \end{aligned} \tag{11}$$

where

$$\boldsymbol{\gamma} = [\gamma(s_1), \gamma(s_2), \ldots, \gamma(s_Q)]^T,$$

$$\mathbf{a}(s_q) = \left[e^{j2k\frac{u_1 s_q}{R_0}}, e^{j2k\frac{u_2 s_q}{R_0}}, \ldots, e^{j2k\frac{u_N s_q}{R_0}}\right]^T. \tag{12}$$

The goal of SAR tomography is to process the data vector $\mathbf{g}$ to recover the back scattering coefficients $\boldsymbol{\gamma}$. Since the positions of the scattering elements are an unknown parameter which needs to be determined, the positions s_q used in forming the vectors $\mathbf{a}(s_q)$ are sampled over a finite range. As a result, the number of satellite passes is usually smaller than the number of discretized positions and the resulting set of linear equations given by (11) is under-determined, i.e., there are an infinite number of solutions. Various approaches have been used to invert the linear system given in (11): Beamforming [5, 6, 7], Nonlinear Least Squares [8], Truncated Singular Value Decomposition (SVD) [9, 8] and Compressive Sensing [10, 11, 12, 13, 8, 14, 15]. For this investigation we have used the compressive sensing approach to recover a sparse vector $\mathbf{a}(s_q)$, i.e., it contains only a few dominant elements. The elevations corresponding to these dominant elements are taken as the elevation estimates of the targets.

Figure 2 shows the positions of the satellite when they do not fall exactly on the u axis. Let r denote the offset between the satellite position and it's projection onto the u axis. The position of the satellite is then given by:

$$\begin{aligned} R(u) &= \sqrt{(R_0 + r)^2 + (u - s)^2}. \\ &= \sqrt{(R_0 + r)^2 + u^2}\sqrt{1 - \frac{2us - s^2}{(R_0 + r)^2 + u^2}} \end{aligned} \tag{13}$$

Using the same approach as before we have:

$$\begin{aligned} R(u) &\approx \sqrt{(R_0 + r)^2 + u^2}\left(1 - \frac{us}{(R_0 + r)^2 + u^2}\right) \\ &\approx \sqrt{(R_0 + r)^2 + u^2} - \frac{us}{R_0}, \end{aligned} \tag{14}$$

where we have assumed that $r \ll R_0$. Thus the case of satellites not falling exactly on the u axis can be handled by modifying the reference range to $R_{ref}(u) = \sqrt{(R_0 + r)^2 + u^2}$.

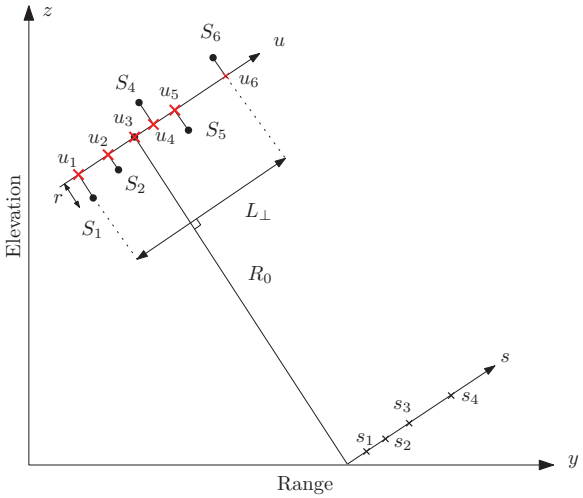

Figure 2: *Tomography geometry with irregular satellite orbits. The black dots denote the satellite orbits, and the red x's denote the satellite's projection onto $L_\perp$ (the perpendicular baseline).*

2.1 Coherence

The development of the signal model so far has ignored noise contributions. In general, the phase of the received signal g_n (10) can be written as:

$$\phi_n = \angle \left(\sum_{m=1}^{Q} \gamma(s_q) e^{j2k\frac{u_n s_m}{R_0}} \right) + \phi_a + \phi_o + \phi_\eta, \tag{15}$$

where $2k\frac{us_q}{R_0}$ is the phase response due to the qth scatterer on the s axis, $\angle()$ denotes the overall angle of the Q components, ϕ_a represents unwanted components due to atmospheric variations between the collection passes, ϕ_o represents the unknown orbital inaccuracies of the collection passes, and ϕ_η is associated with noise contributions such as decorrelation due to speckle and changes of the back-scattering response over time (temporal decorrelation). The phase terms contribute to a multiplicative noise component in the model and as such cannot be overcome by simply increasing the signal to noise ratio, i.e., the effect of the noise is directly proportional to the strength of the back scatterers. An analysis of effects of different types of phase noise on SAR imagery is given in [16], and an analysis specific to tomography is provided in [17, 18].

3 Compressive sensing

The original motivation for compressive sensing was to solve the under-determined system of equations $\mathbf{A}\boldsymbol{\gamma} = \mathbf{g}$ for the solution $\hat{\boldsymbol{\gamma}}$ that contains the smallest number of elements. The problem can be stated as:

$$\hat{\boldsymbol{\gamma}} = \arg\min_{\boldsymbol{\gamma}} \|\boldsymbol{\gamma}\|_0 \text{ subject to } \mathbf{g} = \mathbf{A}\boldsymbol{\gamma}. \tag{16}$$

In the noisy data case we would like to solve:

$$\hat{\boldsymbol{\gamma}} = \arg\min_{\boldsymbol{\gamma}} \|\boldsymbol{\gamma}\|_0 \text{ subject to } \|\mathbf{A}\boldsymbol{\gamma} - \mathbf{g}\|_2 \leq \sigma. \tag{17}$$

However, the solution to this problem is computationally complex and does not have an efficient solution. The difficulty arises because the l_0 norm is neither differentiable nor continuous. The approach taken by [19, 20, 21, 22, 23] is to reformulate the problem as:

$$\hat{\boldsymbol{\gamma}} = \arg\min_{\boldsymbol{\gamma}} \|\boldsymbol{\gamma}\|_1 \text{ subject to } \mathbf{g} = \mathbf{A}\boldsymbol{\gamma}. \tag{18}$$

in the noise free case, and as:

$$\hat{\boldsymbol{\gamma}}_\sigma = \arg\min_{\boldsymbol{\gamma}} \|\boldsymbol{\gamma}\|_1 \text{ subject to } \|\mathbf{A}\boldsymbol{\gamma} - \mathbf{g}\|_2 \leq \sigma, \tag{19}$$

in the presence of noisy measurement data. The application of the l_1 norm on the solution vector promotes sparsity in the components, i.e., there tend to be only a few large elements in the solution vector. The problem given in (18) is referred to as the Basis Pursuit (BP) problem and can be solved using linear programming techniques [24]. The formulation in (19) is referred to as the Basis Pursuit De-Noising (BPDN) problem [24]. Notice that this formulation is dependent on the parameter σ which needs to be determined. The choice of the parameter is obviously dependent on the amount of expected noise in the measurement vector. The choice of σ indirectly affects the solution vector.

Alternate equivalent expressions for the optimization problem given in (19) are:

$$\hat{\boldsymbol{\gamma}}_\lambda = \arg\min_{\boldsymbol{\gamma}} \lambda \|\boldsymbol{\gamma}\|_1 + \|\mathbf{A}\boldsymbol{\gamma} - \mathbf{g}\|_2^2, \tag{20}$$

and

$$\hat{\boldsymbol{\gamma}}_\tau = \arg\min_{\boldsymbol{\gamma}} \|\mathbf{A}\boldsymbol{\gamma} - \mathbf{g}\|_2 \text{ subject to } \|\boldsymbol{\gamma}\|_1 \leq \tau, \tag{21}$$

Utilizing the theory of Lagrange multipliers the constrained problem (19) can be turned into an unconstrained minimization problem given by (20). If the correct value of λ is chosen then the solution to (20) will yield the same solution as (19). The formulation given in (20) is referred to as the l_1 penalized quadratic program [25]. An

equivalent formulation given in (21) places the constraint on the l_1 norm of the solution vector and minimizes the l_2 norm of the reconstruction error. This formulation is referred to as the Least Absolute Shrinkage and Selection Operator (LASSO) and is commonly seen in the statistics community [26]. Although the three formulations of the problem have equivalent minimizations, it is not necessarily straight forward to map the parameter from one formulation into parameters for the other two. However, once a solution to one of the minimization problems has been found the parameters for the other formulations can be determined [25, 27, 28]. The three formulations given in (19), (20), and (21) are convex optimization problems that can be solved efficiently using iterative techniques. Parker et al. [25] provides an overview of many of the approaches used for solving these problems.

Given the equivalent problem formulations in (19), (20) and (21) there are several issues which need to be discussed. The first issue is what value of the parameter in each of these problems should be used. Examining (21) it is immediately apparent that the choice of the parameter τ controls the sparsity of the reconstructed vector, since this l_1 norm constraint appears explicitly in the problem formulation. Alternatively we can examine the choice of the λ parameter in (20). If we choose $\lambda = 0$, then the problem defaults to the under-determined least squares problem. The usual solution to this problem often results in a solution vector which contains a large number of coefficients with non-zero values [23]. On the other hand, as $\lambda \to \infty$ the solution vector $\hat{\boldsymbol{\gamma}}_\lambda \to 0$. As we vary the value of λ from $0 \to \infty$, the solution goes from being dense (non-sparse) to the most sparse vector possible, i.e., $\hat{\boldsymbol{\gamma}}_\lambda = 0$. Clearly, choosing an appropriate value of λ requires some knowledge of the desired sparsity of the solution. An alternative viewpoint comes from examining the σ parameter in the formulation (19). In this formulation, the parameter σ corresponds to l_2 error in the reconstruction vector. Consider the situation where we have already found the solution vector $\hat{\boldsymbol{\gamma}}_\sigma$ for a given noise vector $\mathbf{e}$, i.e.,:

$$\mathbf{A}\hat{\boldsymbol{\gamma}}_\sigma = \mathbf{g} + \mathbf{e}. \tag{22}$$

If the equation is simply scaled (keeping the signal to noise ratio constant) then this requires choosing a larger value of σ to solve this modified problem and achieve the original solution vector. In other words, the choices of the parameters σ, λ, τ are affected by the noise power of the problem rather than just the signal to noise ratio.

A second issue with the compressive sensing approach is solution bias. Examining the two terms of the minimization function in (20), the first term, $\lambda \|\boldsymbol{\gamma}\|_1$, reduces the l_1 norm of the solution vector while the second term models how well the solution vector fits the data. The presence of the l_1 norm term biases the estimate of the solution [29, 30, 31]. In general, the support of the solution is correct but the amplitudes of the elements tend to be underestimated in order to reduce the cost of the l_1 norm. In compressive sensing applications where the amplitude information is not required

this can be neglected. If unbiased estimates of the amplitudes are required, then a debiasing technique can be applied [29, 30, 31].

A third issue with the compressive sensing formulation given in (19), (20) and (21) is that the user must discretize the search space, i.e., choose the spacing of the column vectors in the matrix $\mathbf{A}$. If too few column vectors are used then the reconstruction error is large and the elevation resolution suffers. If too many closely spaced vectors are used then the column vectors in $\mathbf{A}$ become correlated which can introduce spurious peaks and/or sidelobe type behaviour in the solution vector [30]. Numerous metrics have been developed for the matrix $\mathbf{A}$ to provide bounds on the reconstruction error. The most well-known metric is the Restricted Isometry Property (RIP) [19, 32]. The RIP of the matrix $\mathbf{A}$ requires that all the sub-matrices consisting of the columns of the matrix $\mathbf{A}$ are near-isometries. For a matrix satisfying the RIP there are error bounds on a sufficiently sparse reconstruction in the presence of noise. The RIP is a sufficient condition but not a necessary one for sparse reconstruction. Unfortunately, the calculation of the RIP is combinatorially complex and is usually more complex than solving the original compressive sensing problem. A detailed discussion of the RIP and its associated bounds on reconstruction is beyond the scope of the current work; a more detailed description is provided in [19, 32, 33, 34]. Alternatives metrics to the RIP include the mutual coherence and the Null Space Property [33, 34, 35]. The mutual coherence metric is relatively easy to calculate but it provides an overly pessimistic bound on the recovery error. The Null Space property is similar to the RIP in that it is also computationally intensive to calculate.

A more general alternative methodology of analyzing the reconstruction properties in compressive sensing is to assume that errors are present in the model as well as in the observations. Now the modeling equation can be written as:

$$\begin{aligned} \mathbf{A}\hat{\boldsymbol{\gamma}} &= \mathbf{g} + \mathbf{e} \\ (\hat{\mathbf{A}} + \mathbf{E})\hat{\boldsymbol{\gamma}} &= \mathbf{g} + \mathbf{e}, \end{aligned} \tag{23}$$

where $\hat{\mathbf{A}}$ represents the error-free modeling matrix and $\mathbf{E}$ represents the unknown modeling error. When the objective function is the minimization of the Frobenius norm of the errors, i.e., $\|\mathbf{E}\,\mathbf{e}\|_F$, this problem is referred to as the Total Least Squares (TLS) problem [36, 37]. The impact of modeling errors on the solution to compressive sensing formulations appears in [37, 38, 39, 40]. Introduction of the modeling error complicates the process of finding sparse solutions because the problem is no longer convex and modifications to the minimization routines are necessary [41, 42, 43].

4 Analysis and simulation

In this study we are interested in tomographic processing for satellite geometries similar to those of RADARSAT-2 and the RCM. The orbital information used is taken from Analytical Graphics Inc.'s (AGI) Systems Toolkit (STK) software and using historical ephemeris data for RADARSAT-2. Figure 3 illustrates a generic satellite geometry. The origin of the coordinate system is taken at the target of interest at 0 elevation. The elevation angle θ is measured from a local tangent plane at the target. The satellite positions are shown as the blue x's and their projections onto the u axis are shown as black dots. It should be noted that the distribution of the satellite orbits for coherent passes[1] often do not fall along the u axis, i.e., perpendicular to the line of sight, but rather at some angle to it. This effectively reduces the length of the synthetic aperture created by the multiple satellite passes.

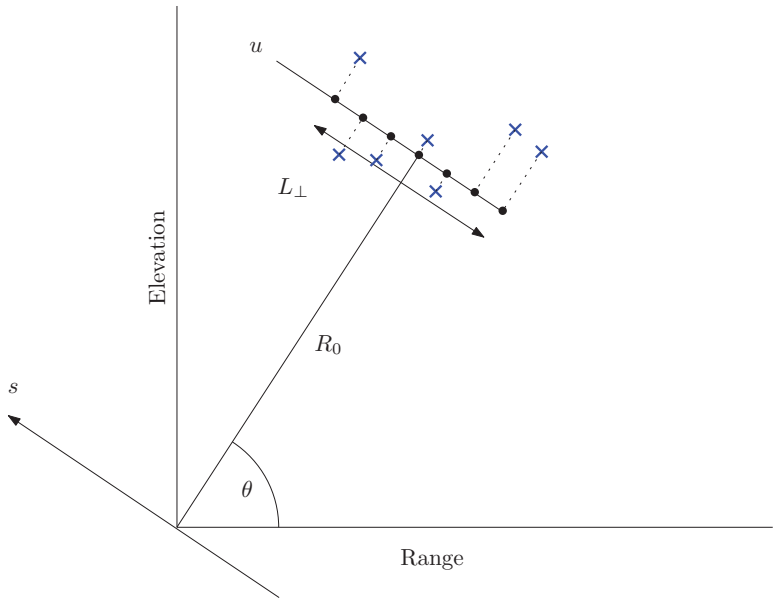

Figure 3: *Generic satellite geometry.*

The first geometry uses eight coherent passes over the area of Ottawa, Canada starting on June 17, 2013. It should be noted that coherent passes for RADARSAT-2 occur every 24 days. The mean elevation angle for these passes is 65.32° and the mean distance to the satellite is 868 km. Figure 4 illustrates the variation of the satellite geometries over the eight passes. The blue x's show the actual satellite position, while the red circles indicate the projection of these positions onto the perpendicular baseline. In this geometry the size of the perpendicular baseline is 439 m. The ellipse shows the variance of the orbital passes in the range and altitude directions. This

[1] Coherent satellite passes are satellite passes which follow the same orbital path. Small deviations in elevation are acceptable.

type of mismatch is likely to occur in practice since the true target heights will not be known apriori.

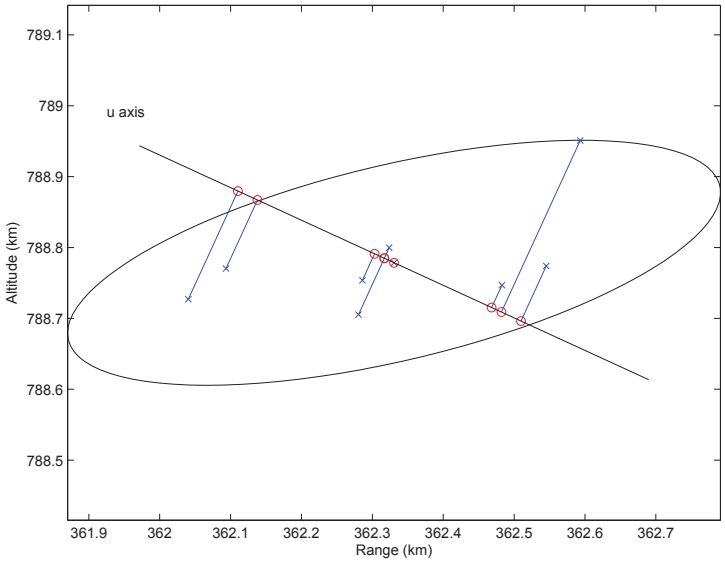

Figure 4: *Geometry 1—satellite geometry for eight orbits. Elevation* = 65.32°. *Perpendicular baseline 439 m.*

The second geometry also uses eight coherent passes over Ottawa, but with a mean elevation angle of 45.27° and mean distance to the satellite of 1067.4 km. The orbital information for the eight passes was obtained from STK for coherent passes starting on June 4, 2013. Figure 5 illustrates the variation of the satellite geometries over these eight passes. Once again, the blue x's represent the actual satellite position, while the red circles indicate the projection of these positions onto the perpendicular baseline. In this geometry the length of the perpendicular baseline is only 298 m.

Since the interval for coherent data passes for RADARSAT-2 is 24 days, the data collection duration for the eight passes is 168 days. It is expected that this duration would introduce both temporal and atmospheric incoherence throughout most of the SAR scene and therefore only strong persistent scatterers will be of interest. The use of only eight measurements to resolve two or more closely spaced persistent scatterers is a challenging scenario. Therefore, two additional geometries were simulated. The third geometry is exactly same as the first geometry except that an additional 23 orbits were randomly generated using the original 8 orbits as a basis for a Gaussian distribution. This produces a total of 31 orbital passes. Figure 6 illustrates the satellite geometries for these orbits. Due to additional satellite passes, the perpendicular baseline in this geometry is extended to 785 m. Similarly, the forth geometry is exactly same as the second geometry with an additional 23 randomly generated orbits. The geometries for these orbits are shown in Figure 7. The perpendicular baseline in this geometry is

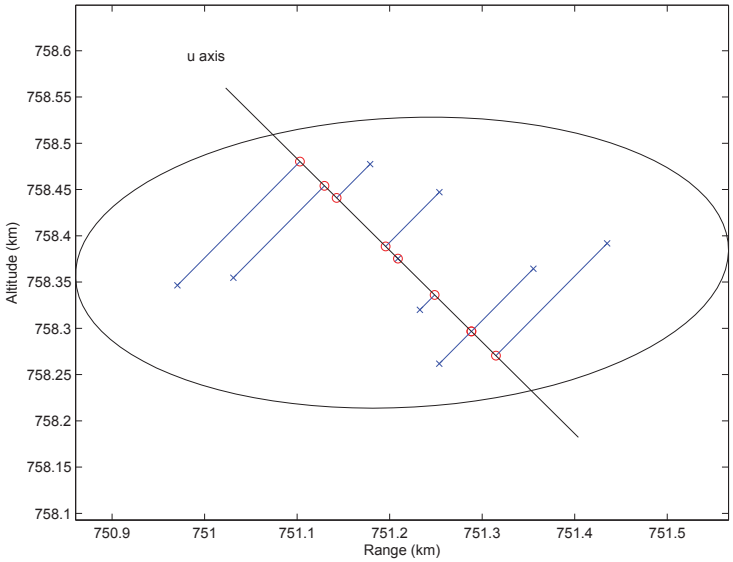

Figure 5: *Geometry 2—satellite geometry for eight orbits. Elevation* = 45.27°. *Perpendicular baseline 298 m.*

444 m. These last two geometries are more typical of the expected RCM geometries where coherent data collections will be available approximately every eight days.

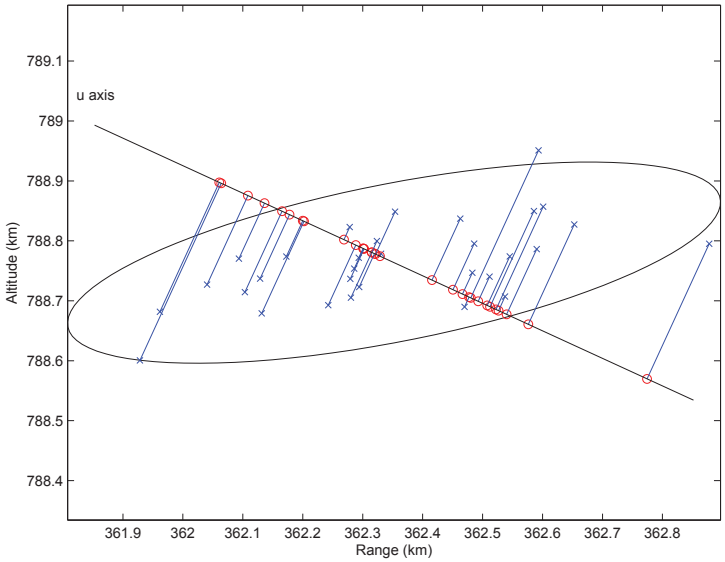

Figure 6: *Geometry 3—satellite geometry for 31 orbits. Elevation* = 65.32°. *Perpendicular baseline 785 m.*

For the work conducted under this investigation the Fast Iterative Shrinkage Thresh-

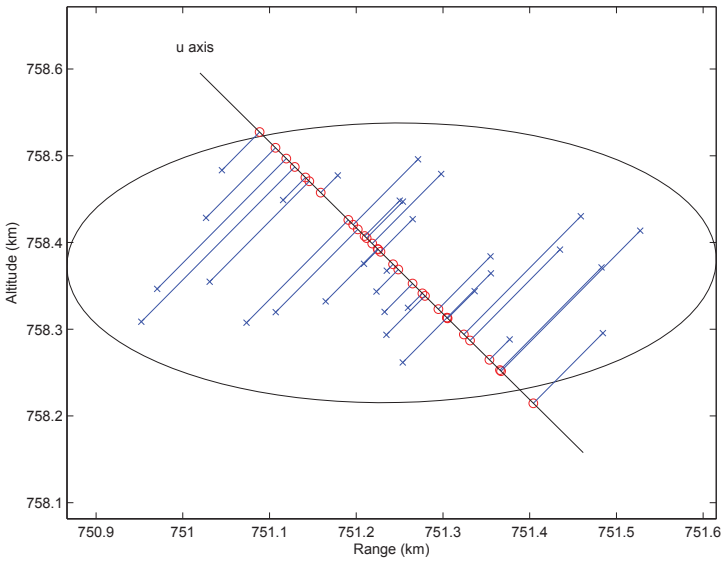

Figure 7: *Geometry 4—satellite geometry for 31 orbits. Elevation* $= 45.27°$. *Perpendicular baseline* 444 *m.*

olding Algorithm (FISTA) [25, 44] was used to solve the penalized quadratic program formulation (20). A summary of the FISTA algorithm is given in Annex B. The FISTA algorithm was chosen because it is fairly easily to implement and it is widely used across the compressive sensing community. We have also assumed that the targets are perfectly coherent and that there is no phase noise. The elevation estimates are taken from the corresponding elevations of the dominant elements in the recovered vector $\boldsymbol{\gamma}$. The elevation grid for the $\boldsymbol{A}$ matrix is discretized from -10 m to 100 m in steps of 0.55 m. The elevation grid is kept fixed throughout all the simulations. This fixed grid introduces a modeling error due to the mismatch between the discretized elevation and the true height of the target.

In order to evaluate the performance of the compressive sensing approach to tomography, it is useful to have the theoretical performance limits such as the Rayleigh resolution and the Cramer-Rao Lower Bound (CRLB) of the elevation estimates. The Rayleigh resolution (null to null) is relatively straight forward to calculate; the null to null beamwidth of the synthetic aperture in elevation is $\frac{\lambda}{2L_\perp}$. Therefore, at a range of R_0 meters the Rayleigh resolution (ρ_s) is given as:

$$\rho_s = \frac{\lambda R_0}{2L_\perp}, \tag{24}$$

where ρ_s denotes the resolution along the s axis. The corresponding resolution in elevation is given by:

$$\rho_h = \frac{\lambda R_0}{2L_\perp} \sin\theta, \tag{25}$$

where ψ is the elevation angle. Table 1 illustrates the Rayleigh resolution for the four geometries discussed above.

Table 1: *Rayleigh resolution for RADARSAT-2 type geometries.* $\lambda = 0.0555$ *m.*

Geometry	$L_\perp$	R_0	ρ_s	ρ_h
Geometry 1	439 m	868 km	54.87 m	49.86 m
Geometry 2	298 m	1067 km	99.36 m	70.59 m
Geometry 3	785 m	868 km	30.68 m	27.88 m
Geometry 4	444 m	1067 km	66.69 m	47.38 m

The formulas for the Cramer-Rao bound of the elevation estimate presented in this section are taken from Zhu [30] and Swingler [45] and were derived empirically. While numerical calculation of the bound can be done in the specific case, it is these empirical formulas which provide general insight to the behaviour of the system. It should also be remembered that the Cramer-Rao bound is a theoretical lower limit and may not be achievable in practice. The asymptotic (high Signal to Noise ratio (SNR) approximation) Cramer-Rao lower bound of the elevation estimate for a single target at the position s_q is given by:

$$\sigma_{s_q,0} = \frac{\lambda R_0}{4\pi\sqrt{2} \cdot \sqrt{N \cdot SNR_q}\sigma_b}, \tag{26}$$

where N is the number of satellite passes, SNR_m is the signal to noise ratio of the individual scatter, and σ_b is the standard deviation of the perpendicular baseline. Note that the 0 in the subscript of $\sigma_{s_q,0}$ is used to denote the single target case and distinguish it from the two target case examined later on. For uniformly distributed baseline (either a uniform random distribution or equally spaced), $\sigma_b = L_\perp/\sqrt{12}$ and thus $\sigma_{s_q,0}$ can be related to the resolution by:

$$\begin{aligned} \sigma_{s_q,0} &= \frac{\lambda R_0\sqrt{12}}{4\pi\sqrt{2} \cdot \sqrt{N \cdot SNR_q}L_\perp}, \\ &= \sqrt{\frac{3}{2}}\frac{\rho_s}{\pi \cdot \sqrt{N \cdot SNR_q}}. \end{aligned} \tag{27}$$

Figure 8 plots the Cramer-Rao bound of the elevation estimate normalized by the resolution as a function of $N \cdot SNR_q$ in the single scatterer case. From the graph it is straightforward to see that the estimation bound is going to be on the order of 1/100th - 1/5th of the resolution cell size for the most practical values of $5 \leq N \cdot SNR_q \leq 35$. Table 2 calculates the Cramer-Rao bound of the elevation estimate for a single scatterer at various SNRs for each of the four simulation geometries.

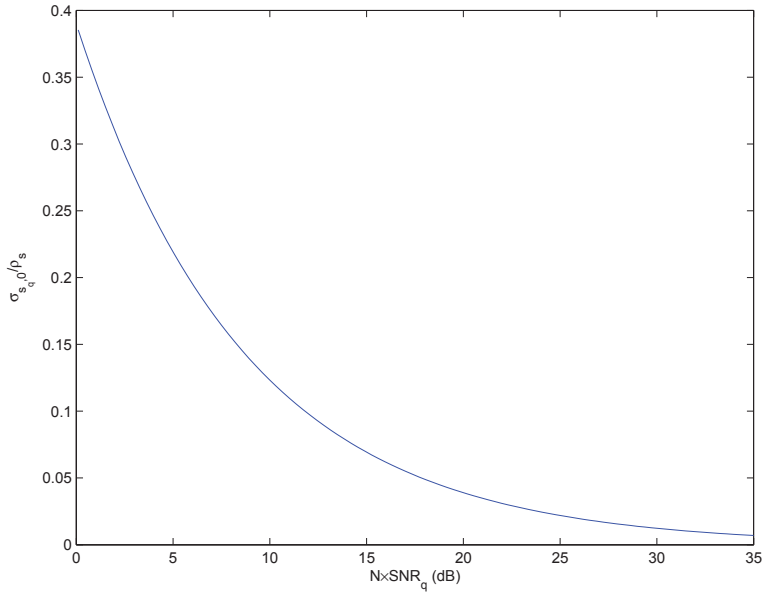

Figure 8: *CRLB $\sigma_{s_q,0}$ of the elevation accuracy of a single scatterer normalized by the resolution ρ_s as a function of $N \cdot SNR_q$.*

Table 2: *Cramer-Rao bounds for elevation estimates of a single target for the various simulation geometries.*

Geometry	N	SNR=5 dB	SNR=10 dB	SNR=20 dB
Geometry 1	8	$\sigma_{s_q,0} = 4.25$ m	$\sigma_{s_q,0} = 2.39$ m	$\sigma_{s_q,0} = 0.76$ m
Geometry 2	8	$\sigma_{s_q,0} = 7.7$ m	$\sigma_{s_q,0} = 4.33$ m	$\sigma_{s_q,0} = 1.37$ m
Geometry 3	31	$\sigma_{s_q,0} = 1.2$ m	$\sigma_{s_q,0} = 0.68$ m	$\sigma_{s_q,0} = 0.21$ m
Geometry 4	31	$\sigma_{s_q,0} = 2.63$ m	$\sigma_{s_q,0} = 1.48$ m	$\sigma_{s_q,0} = 0.47$ m

We are also interested in the Cramer-Rao lower bound of the elevation estimates in the case of two targets. For simplicity it is assumed that the two targets have the same SNR. It is noted that if the two targets are sufficiently separated then the lower bound is essentially the same as the single-target case [46, 45]. In the case of two closely spaced targets, the CRLB for position error is approximated by:

$$\sigma_{s_q} = c_0 \sigma_{s_q,0}, \tag{28}$$

where $\sigma_{s_q,0}$ is the CRLB of the elevation estimate of the qth scatterer in the absence of the other scatterer given in (27), and c_0 is a proximity factor which describes the impact of the presence of the other scatterer. Examination of (28) reveals that c_0 can be treated as the normalized CRLB, where the normalization is done with respect to the CRLB of the single target scenario. The formula for c_0 is modeled after [45] and

is given by:

$$c_0^2 = \max\left\{\frac{40\alpha(1-\alpha/3)}{9-6(3-2\alpha)\cos\left(2\Delta\varphi+2\pi\alpha(\frac{2\delta_L}{L_\perp}-\frac{1}{N})\right)+(3-2\alpha)^2}, 1\right\} \tag{29}$$

where $\alpha = \delta_s/\rho_s$ is the distance between the two scatterers normalized by the Rayleigh resolution, $\Delta\varphi$ is the phase difference between the two targets, δ_L is the center position of the elevation aperture and the elevation aperture is $[-L\perp/2,\ L_\perp/2]$. For our purposes we have taken $\delta_L = 0$. Figure 9 shows the normalized CRLB standard deviation as a function of the normalized target separation distance for different phase differences between the targets. When the target separation distance is larger than the Rayleigh resolution, the presence of the second target has very little influence on the CRLB of the estimates of target elevations. As the targets move closer together, the presence of the second target has a larger effect on the deviation of the elevation estimate. The presence of the second target has the smallest effect on the deviation of the estimate when $\Delta\varphi = \pi/2$ and the largest effect on the deviation when $\Delta\varphi = 0$.

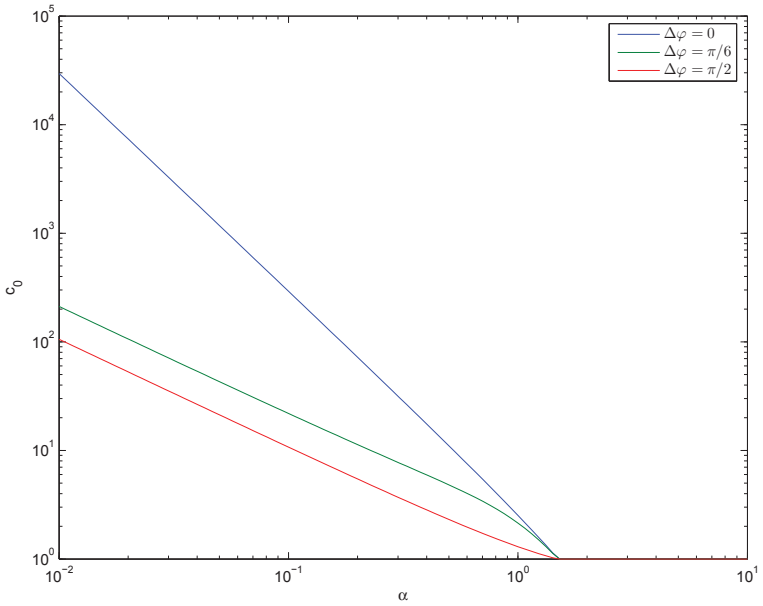

Figure 9: *Normalized CRLB, c_0, of the elevation accuracy of two scatterers as a function of the normalized distance α between the scatterers for different values of the phase difference between the scatterers.*

The behaviour of (29) depends non-linearly on several parameters (target phase, distance between the targets and the number of measurements); the following graphs demonstrate the behaviour of the normalized CRLB as these parameters are varied. Figure 10 shows c_0 as a function of the number of data acquisitions for a number of different target phase differences. Figure 11 shows c_0 as a function of the scatterer phase difference $\Delta\varphi$, for a few different normalized target separation values α.

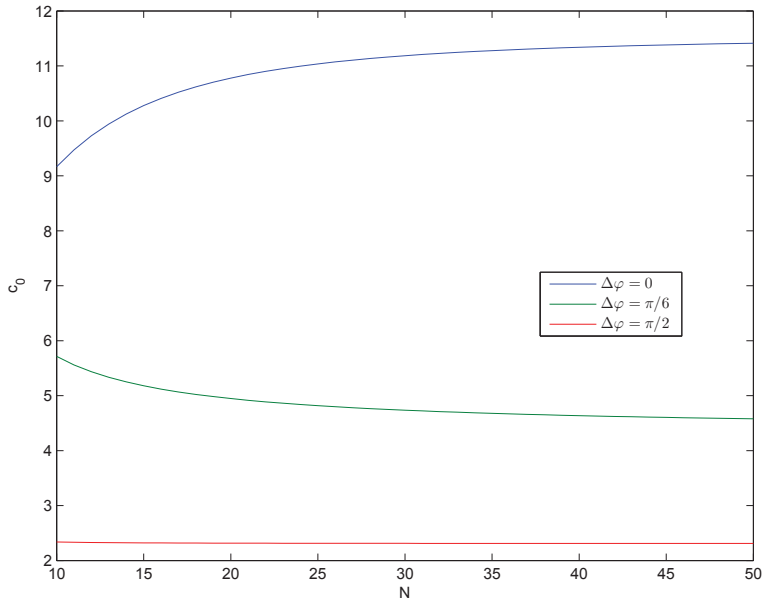

Figure 10: *Normalized CRLB, c_0, of the elevation estimates of two scatterers as a function of the number of measurements N.*

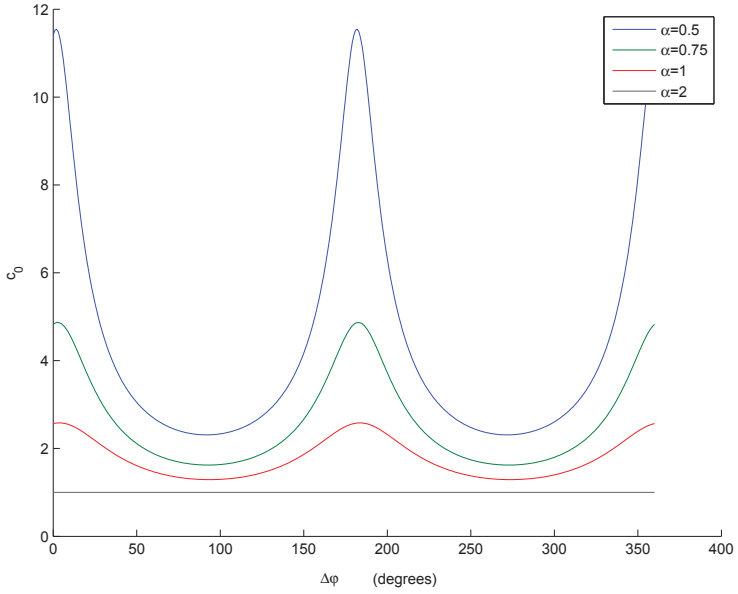

Figure 11: *Normalized CRLB, c_0, of the elevation estimates of two scatters as a function of their phase difference $\Delta\varphi$ for different values of the normalized distance between the scatterers α.*

4.1 Simulation results for Geometry 1 with a single target

In the first simulation there is a single scatterer and the main metrics of interest are the mean and standard deviation of the elevation estimate, which give an idea of the accuracy of the approach. In the simulation, the height of the target is moved from 80 m down to 0 m in steps of 1.9 m. One hundred trials are performed at each elevation. Figure 12 illustrates the mean estimates of the height as a function of the true heights of the target when the SNR=20 dB. At this SNR the mean values of the estimated elevations correspond well to the true heights. Figure 13 shows the standard deviation of the elevation estimates as a function of the true elevation when the SNR=20 dB. The standard deviations vary between 0.3 m and 0.55 m across all the target elevations.

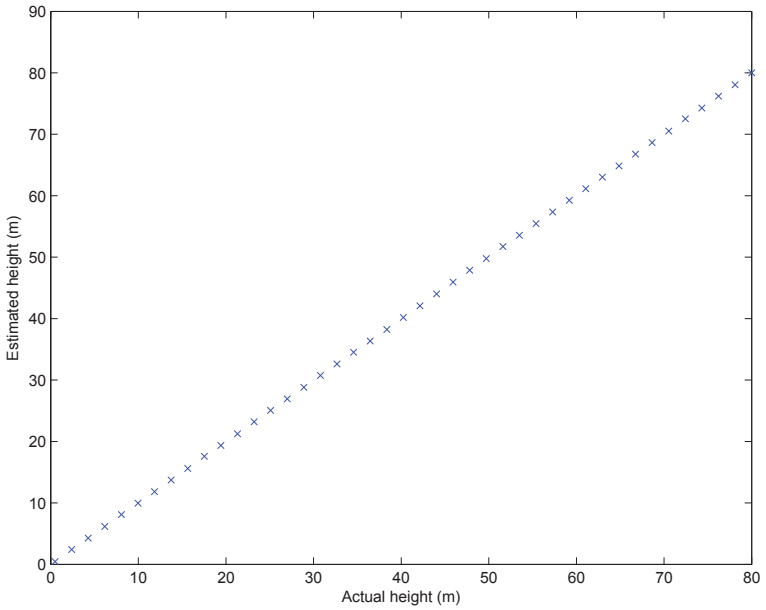

Figure 12: *Mean of estimated height vs. true height for a single target for Geometry 1. SNR=20 dB.*

Figure 14 shows the mean of the elevation estimates vs. the true heights when the SNR is decreased to 10 dB, again the estimates are consistent with true elevations. Figure 15 shows the standard deviations of the elevation estimates when the SNR=10 dB. The standard deviations vary between 0.75 m and 1.1 m across the range of target elevations. As expected, the deviations have increased over the SNR=20 dB scenario.

Figure 16 shows the mean of the elevation estimates vs. the true heights when the SNR is decreased to 5 dB. The estimates are generally consistent with true elevations, but there are a few elevations that appear to have a small bias. Figure 17 shows the standard deviations of the elevation estimates for an SNR of 5 dB. As expected, the deviations have increased over the SNR=10 dB scenario. For most of the target

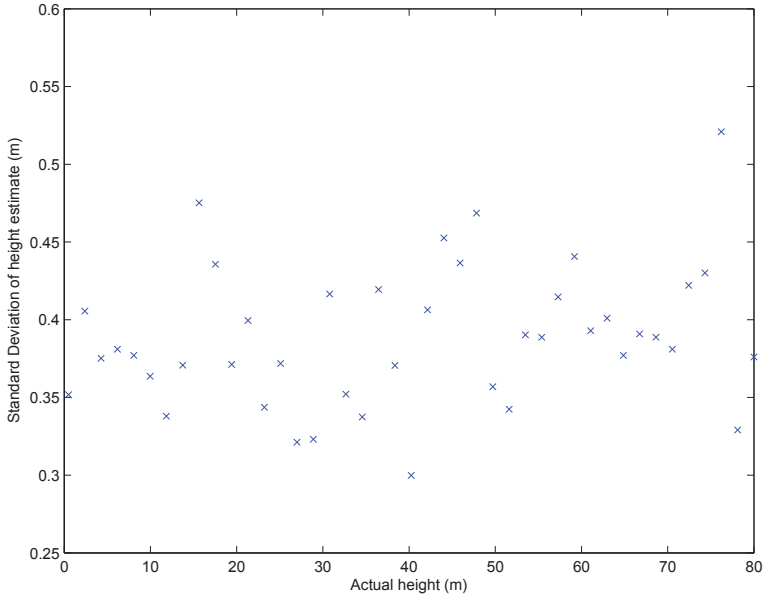

Figure 13: *Standard deviation of the estimated height vs. the true height for Geometry 1. SNR=20 dB.*

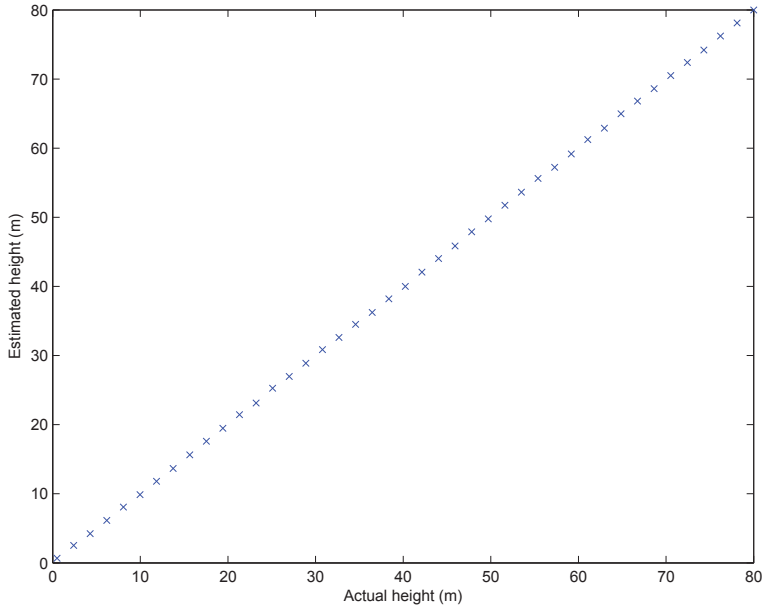

Figure 14: *Mean of estimated height vs. true height for a single target for Geometry 1. SNR=10 dB.*

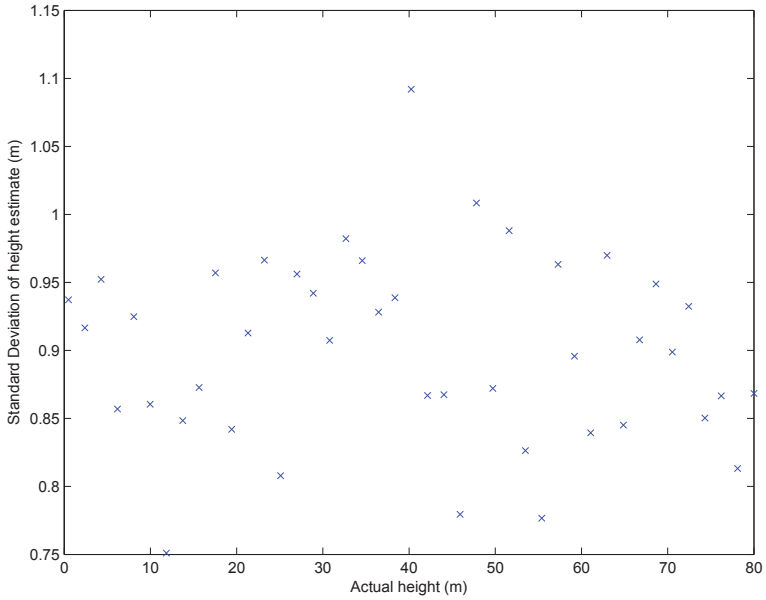

Figure 15: *Standard deviation of the estimated height vs. the true height for Geometry 1. SNR=10 dB.*

elevations the deviations of the estimates are less than 2 m; however, the deviations increase up to 9 m for target elevations in the range 30 m to 60 m.

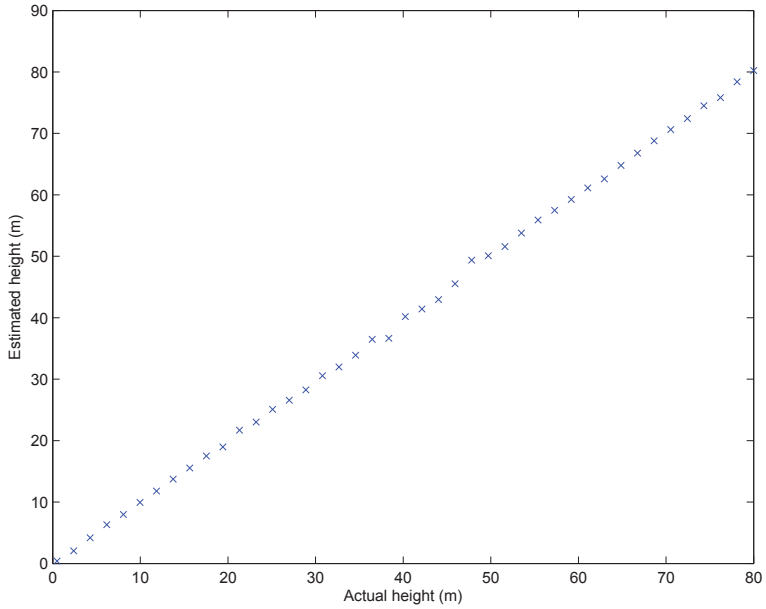

Figure 16: *Mean of estimated height vs. true height for a single target for Geometry 1. SNR=5 dB.*

For ease of comparison, Figure 18 plots the standard deviations of the elevation

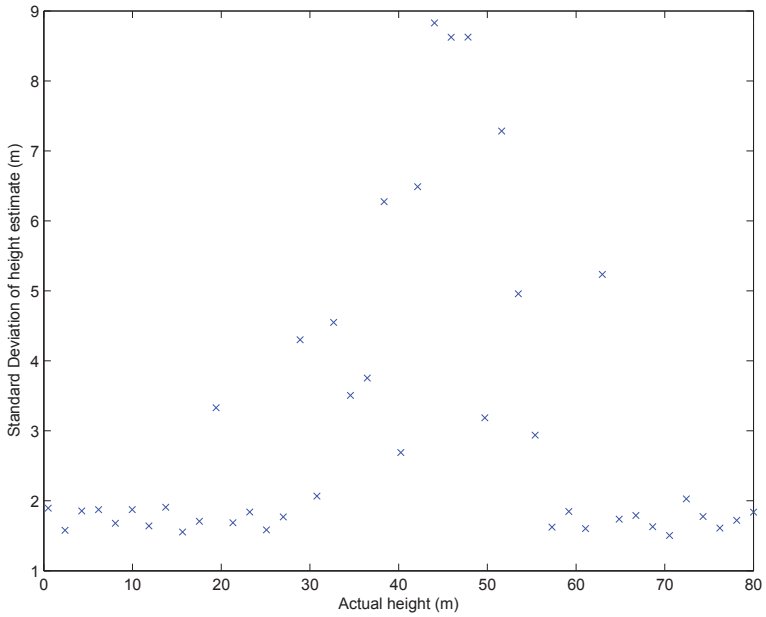

Figure 17: *Standard deviation of the estimated height vs. the true height for Geometry 1. SNR=5 dB.*

estimates for the three different SNRs. From this figure it is easy to see that at SNR=20 dB and SNR=10 dB the CS algorithm performs well. At SNR=5 dB, the deviation of the elevation estimates significantly degrades over the elevation range of 25 m to 60 m.

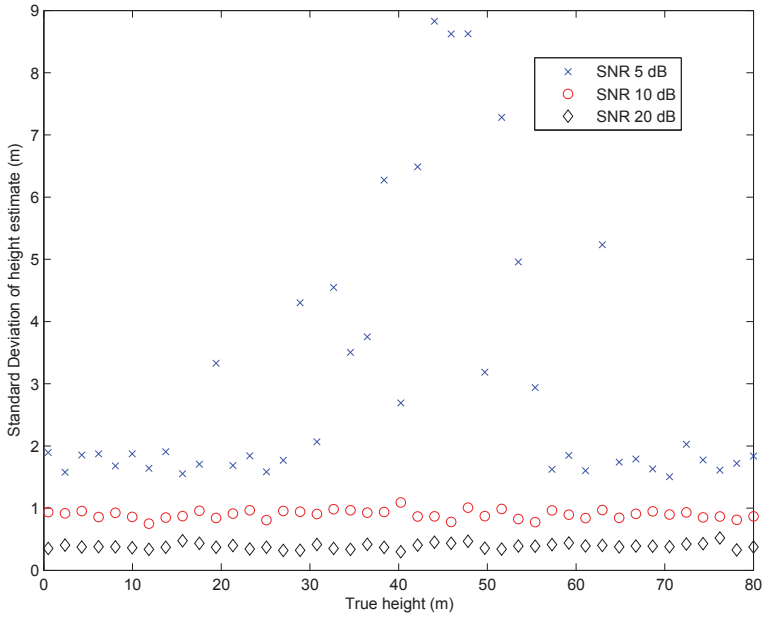

Figure 18: *Standard deviation of the estimated height vs. the true height for Geometry 1.*

4.2 Simulation results for Geometry 2 with a single target

The following set of results is for a single target scenario, but with Geometry 2 as described earlier. Due to the increased range and decreased aperture ($L_\perp$), it is expected that the deviation of the estimates will increase corresponding to (27). Figure 19 illustrates the mean estimates of the height as a function of the true height of the target for Geometry 2 when the SNR=20 dB. At this SNR the mean values of the estimated elevations correspond well to the true heights. Figure 20 shows the standard deviations of the elevation estimates as a function of the true elevation when the SNR=20 dB. The standard deviations of the elevation estimates varies from 0.8 m to 1.7 m across the all the target elevations, and the deviations are higher than for the same SNR in Geometry 1.

Figure 21 shows the mean of the elevation estimates vs. the true heights for Geometry 2 when the SNR is decreased to 10 dB. Again, the estimates are consistent with true elevations. Figure 22 shows the standard deviations of the elevation estimates when the SNR=10 dB. The deviations vary from 2.2 m to 2.9 m across the range of target elevations. As expected, the deviations have increased over the SNR=20 dB scenarios for both Geometry 1 and Geometry 2.

Figure 23 shows the mean of the elevation estimates vs. the true heights when the SNR is decreased to 5 dB, again the estimates are consistent with the true elevations. Figure 24 shows the standard deviations of the elevation estimates for an SNR of

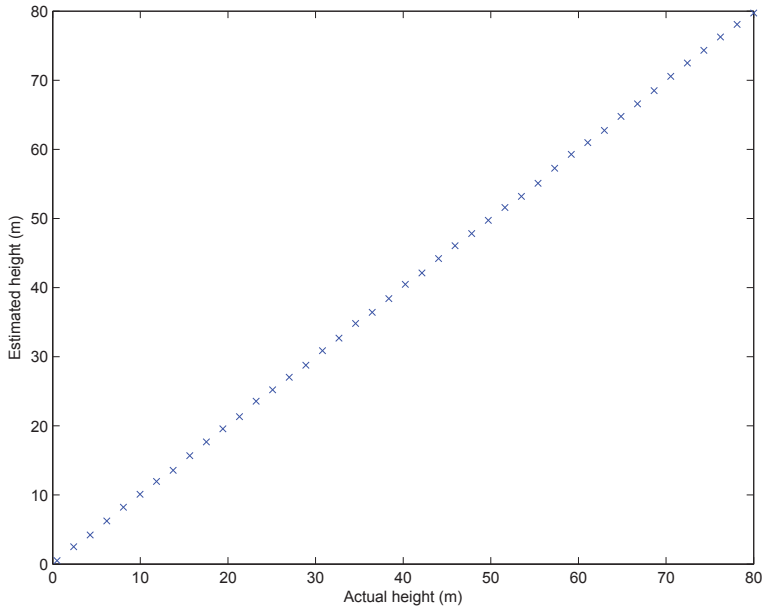

Figure 19: *Mean of estimated height vs. true height for a single target for Geometry 2. SNR=20 dB.*

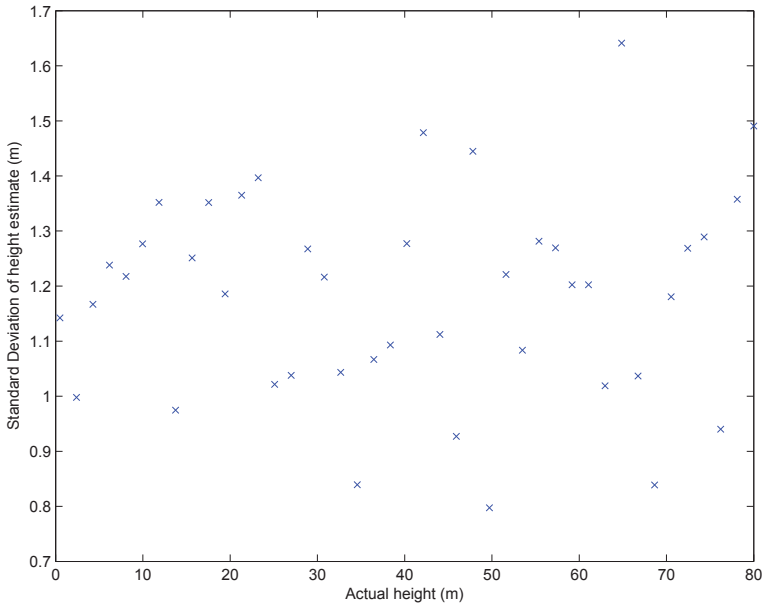

Figure 20: *Standard deviation of the estimated height vs. the true height for Geometry 2. SNR=20 dB.*

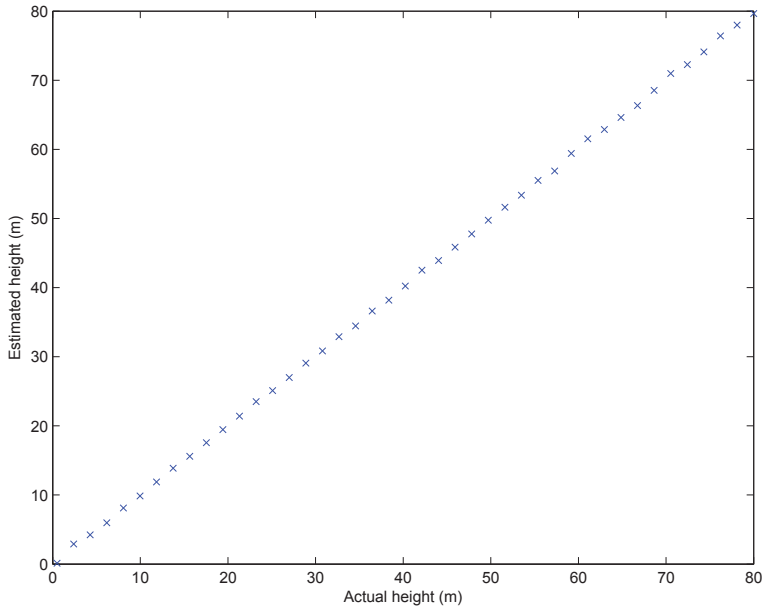

Figure 21: *Mean of estimated height vs. true height for a single target for Geometry 2. SNR=10 dB.*

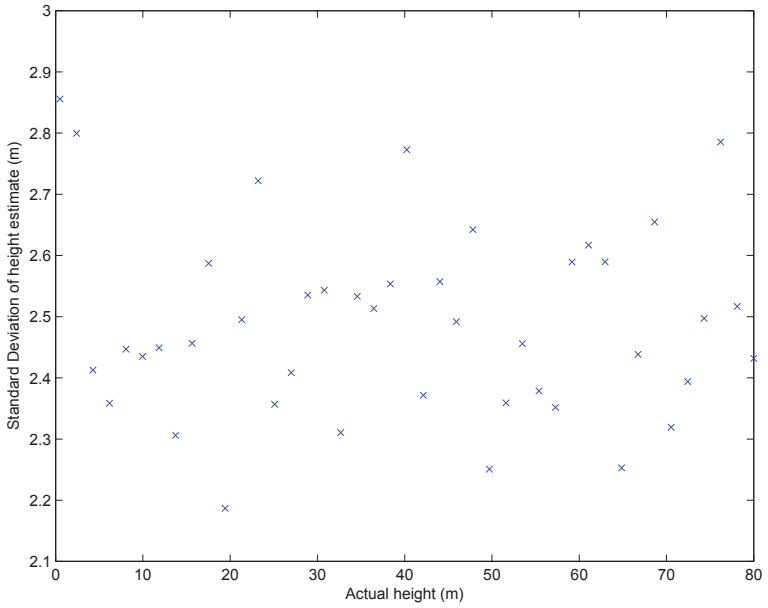

Figure 22: *Standard deviation of the estimated height vs. the true height for Geometry 2. SNR=10 dB.*

5 dB. As expected, the deviations have increased over the SNR=10 dB scenarios for Geometry 1 and Geometry 2. The deviations range from 3.6 m to 5.6 m across the range of target elevations.

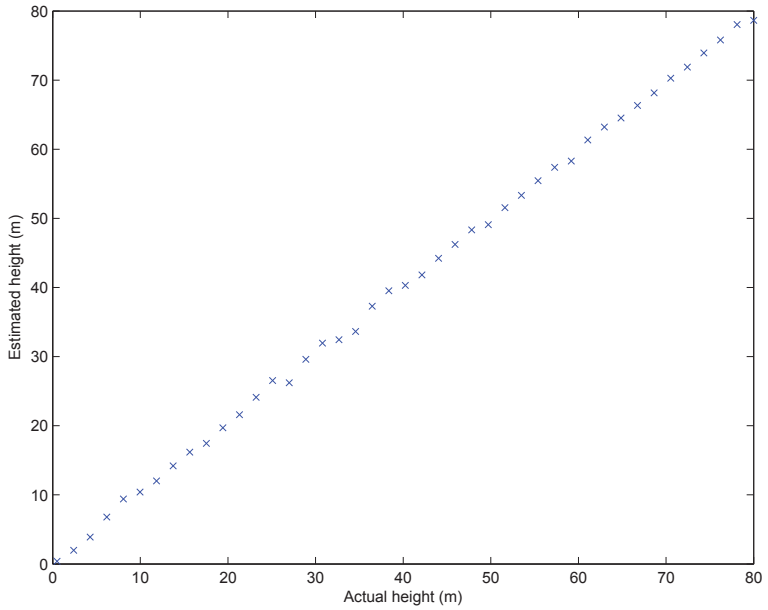

Figure 23: *Mean of estimated height vs. true height for a single target for Geometry 2. SNR=5 dB.*

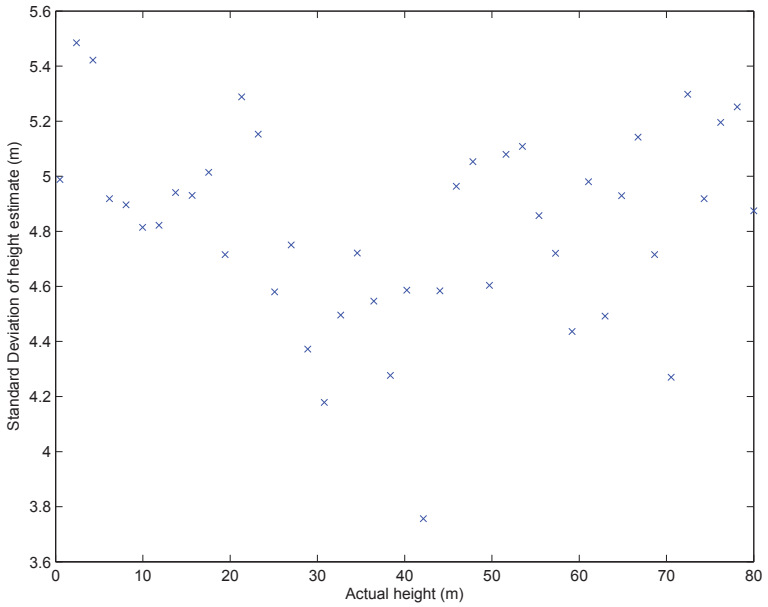

Figure 24: *Standard deviation of the estimated height vs. the true height for Geometry 2. SNR=5 dB.*

Comparing Figure 24 and Figure 17 reveals the different behaviour of the standard deviation of the elevation estimates. For Geometry 2 the standard deviations are below 5.6 m for all the target elevations while for Geometry 1 the bound on the deviations varies depending on the elevation. Since both simulations use the same target elevations and have discretized the elevation grid in the same way, then this difference is not accounted for by the mismatch between the true target elevations and the discretized grid. The performance of the CS reconstruction is dependent on the spacing of the measurements, i.e., the spacing of the satellite orbits.

For ease of comparison, Figure 25 plots the standard deviations of the elevation estimates for the three different SNRs. From this figure it is easy to see how the deviations of the elevation estimates increases as the SNR decreases. In this geometry the estimates do not display the erratic behaviour at SNR=5 dB that was seen in Geometry 1.

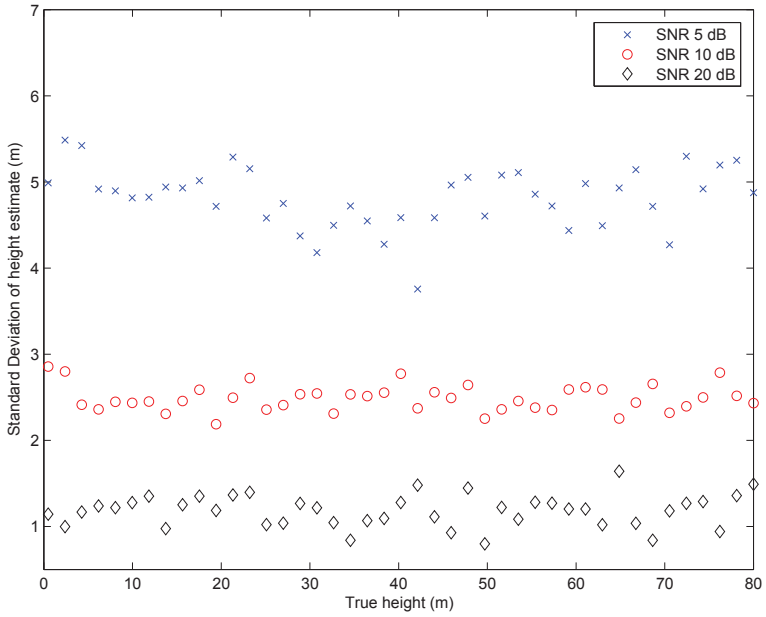

Figure 25: *Standard deviation of the estimated height vs. the true height for Geometry 2.*

4.3 Simulation for Geometry 1 with two targets

The main objective of tomographic processing is to provide resolution in elevation direction. This section presents the results of compressive processing in Geometry 1 for two targets under various signal to noise ratios. The first target is kept at an elevation of 0 m, while the second target is moved in uniform decrements of 1.9 m from an elevation of 80 m down to 0.5 m. At each elevation 100 trials are performed.

The nature of the CS approach tends to produce solution vectors that have a small number of distinct peaks. In order to understand the results presented in the following sections, it is important to understand the way these solution peaks are used in the estimate of the target elevations. The peaks in the solution vector that are closest to the true value of the target elevations are used as the estimate of the target elevation. Consider a couple of examples. If there are two targets but the solution vector only has a single peak, then the elevation corresponding to the peak is used as the elevation estimate for both targets. If the targets are widely separated and the peak is in the middle, then the mean estimate will be biased and the standard deviation of the elevation estimate will be large. If the two targets are close together and the peak is in between them then mean will have less bias and the deviation of the elevation estimate will be small.

In the situation when the solution vector has two peaks, it is still possible for one peak to be used as the estimated elevation for both targets with the similar effects on the mean and standard deviation just described. It is also possible that two different peaks are used for the estimates for the target locations and this usually corresponds to estimated elevations with smaller deviations.

Figure 26 shows the mean estimates of the target elevations for Geometry 1 when the SNR of both targets is 20 dB. The red circles are the mean of the estimates of the target at 0 m elevation. The blue x's are the mean estimates of the elevation of the second target. The elevation estimates are generally consistent with the true values; however, the mean estimates display a small bias at certain target elevations. Comparing Figure 26 with the mean estimate in the case of a single target (Figure 12) reveals that the presence of the second target can result in a small biased estimate of the target elevations.

Figure 27 shows the standard deviations of the estimates of the two target elevations, when the targets' SNR is 20 dB. The red o's denote the values for the target at 0 m elevation and the blue x's denote the values for the second target. The deviations of the estimates are generally less than 2 m until the target separation becomes less than 10 m. Below 10 m in separation, the deviations of the elevation estimates increase linearly with decreasing target separation. It should also be noted that when the two targets are sufficiently close together the deviations of the estimates decrease, i.e., the presence of the second target does not interfere with the estimation algorithm because the CS algorithm is not capable of separating the two closely spaced targets.

It is also noted that in 40 m to 60 m target elevation range, the deviations of the elevation estimate for the target at 0 m remain less than 2 m. Meanwhile, the deviations of the estimate of the other target increases dramatically in this same range. The most likely reason for this variation in the estimates is that this particular geometric distribution of orbits displays an increased sensitivity to this range of elevations. A

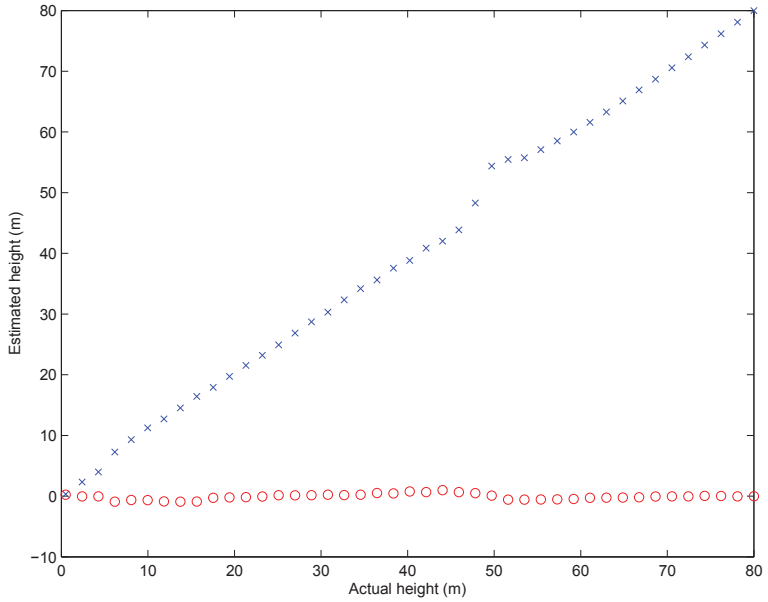

Figure 26: *Mean of estimated heights for two targets in Geometry 1. The SNR for both targets is 20 dB. The elevations are plotted as a function of the true height of the target with the varying elevation.*

similar effect was seen in the single target case when the SNR=5 dB for Geometry 1, but this effect is not seen at any of the SNRs for Geometry 2 in the single target case (see Figure 25) nor is it seen in the two target case for Geometry 2 (see Figures 36, 39 and 42 in Section 4.4). This would indicate that particular geometric distributions of orbits may have difficulty resolving targets at certain elevations.

Figure 28 shows the probability of detecting two distinct targets for Geometry 1 when the targets' SNR is 10 dB. Below 10 m target separation the CS algorithm has difficulty resolving two distinct targets, i.e., only one target is detected and the estimate becomes biased and the deviation increases. The detection probability drops slightly for the target elevation near 50 m, thus at this elevation only one target is detected. If the CS algorithm estimates single target near the 0 m elevation, then this explains why the deviation is higher for the second target.

Figure 29 shows the mean estimates of the target elevations for Geometry 1, when the SNR of both targets is 10 dB. Comparing the means estimates to the SNR=20 dB scenario reveals that the means are consistent with the true values when the targets are widely separated. When the targets are closer than 40 m, the elevation estimates are slightly biased. The target elevation estimates for both targets also display a small bias when the elevated target is near 50 m elevation.

Figure 30 shows the standard deviations of the estimates for the two target elevations, when the targets' SNR is 10 dB. The deviations of the estimates are generally less

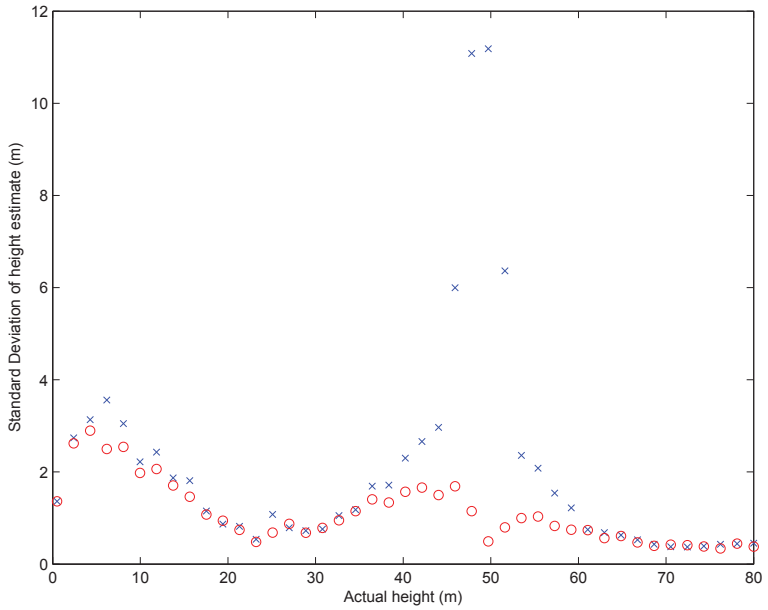

Figure 27: *Standard deviation of estimated heights for two targets in Geometry 1. The SNR for both targets is 20 dB. The deviations are plotted as a function of the true height of the target with the varying elevation.*

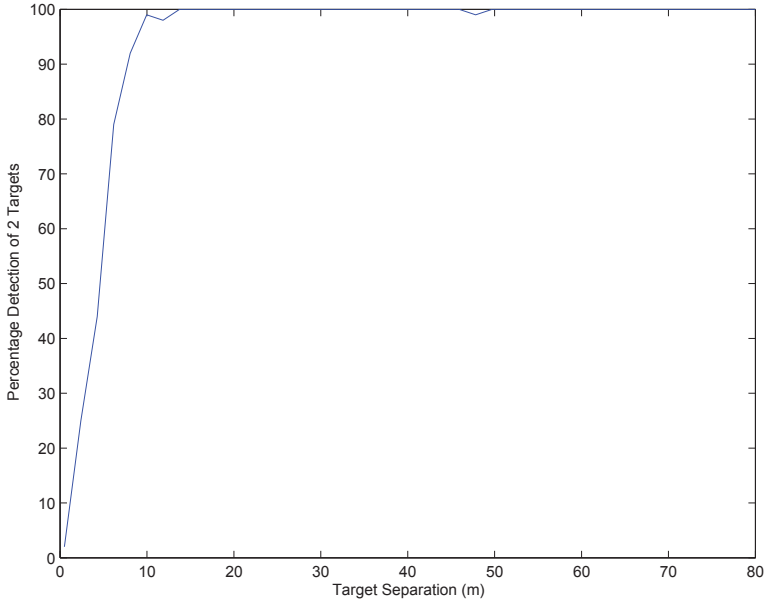

Figure 28: *Probability of detection of two distinct targets in Geometry 1. The SNR of both targets is 20 dB.*

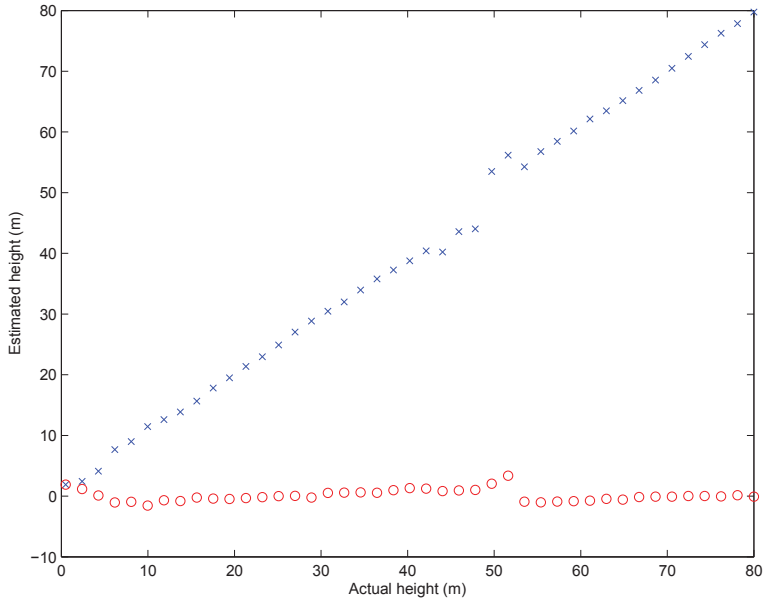

Figure 29: *Mean of estimated heights for two targets in Geometry 1. The SNR for both targets is 10 dB. The elevations are plotted as a function of the true height of the target with the varying elevation.*

than 5 m, except when the elevated target is in the elevation range of 45 m to 55 m, and when the targets are very close in elevation. This is very similar behaviour to the deviations of the elevation estimates when the SNR=20 dB. Figure 31 shows the probability of detecting two distinct targets. Below 25 m target separation the CS algorithm has difficulty resolving two distinct targets. It should be noted that over the elevation range of 45 m to 55 m, the algorithm has difficulty resolving two distinct targets, which would explain the increase in the deviations of the estimates over this elevation range.

Figure 32 shows the mean of the elevation estimates for Geometry 1 when the target SNR is 5 dB. The mean estimates are generally consistent with the true values; however, there do appear to be a few elevations where the mean is biased, e.g., when the elevated target is between 45 m and 55 m in elevation. Figure 33 shows the standard deviations of the elevations estimates of the two targets, when the SNR is 5 dB. In this figure the different behaviour of the deviation of the elevation estimates for each of the two targets becomes apparent. The deviations of the elevation estimate for the target at 0 m are generally less than m over most of the elevations of the second target. The deviations of the elevation estimates for the second target are much greater over the 25 m to 69 m elevation range.

Figure 34 shows the probability of detecting two distinct targets at various elevations when the SNR of both targets is 5 dB. At this SNR level, the detection performance

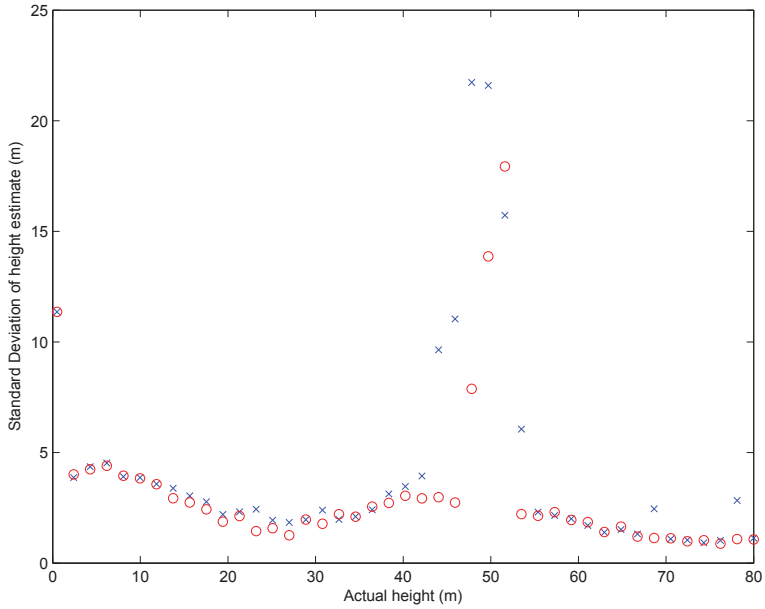

Figure 30: *Standard deviation of estimated heights for two targets in Geometry 1. The SNR for both targets is 10 dB. The deviations are plotted as a function of the true height of the target with the varying elevation.*

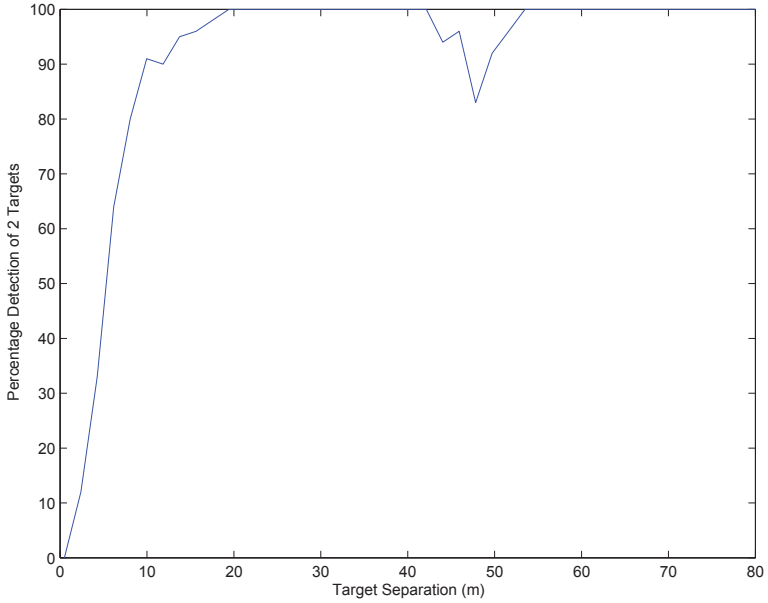

Figure 31: *Probability of detection of two distinct targets as a function of the target separation in Geometry 1. The SNR of both targets is 10 dB.*

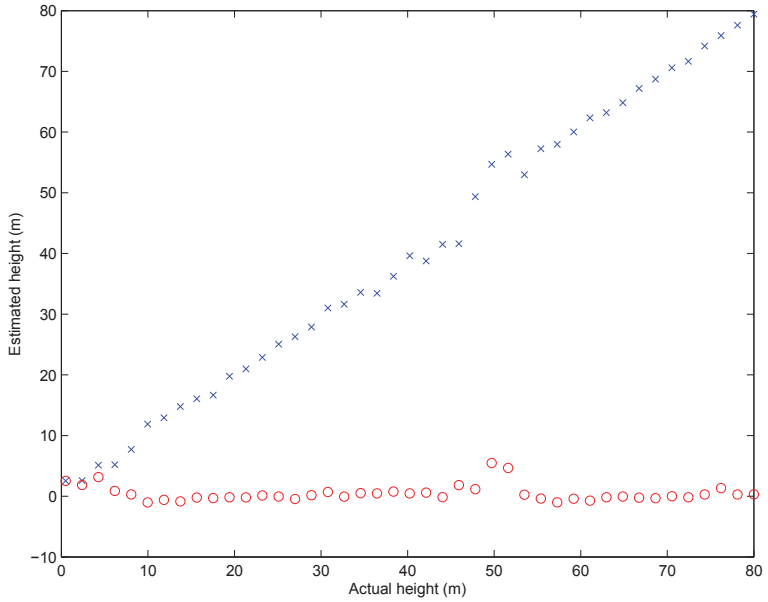

Figure 32: *Mean of estimated heights for two targets in Geometry 1. The SNR for both targets is 5 dB. The elevations are plotted as a function of the true height of the target with the varying elevation.*

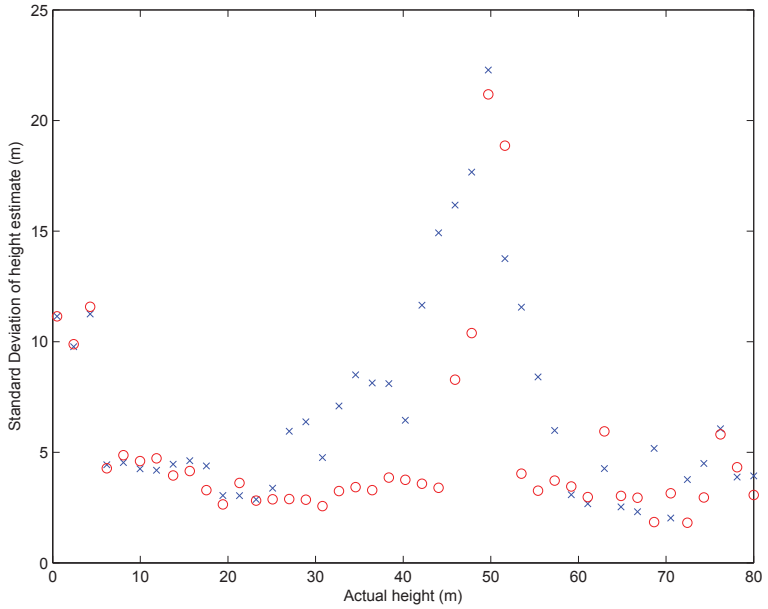

Figure 33: *Standard deviation of estimated heights for two targets in Geometry 1. The SNR for both targets is 5 dB. The deviations are plotted as a function of the true height of the target with the varying elevation.*

of the CS approach to resolve two distinct targets is approximately 90% when the target separation distances range from 12 m to 60 m. The detection performance begins to significantly degrade when the target separation becomes less than 12 m. The detection probability also shows variability over the target elevation range 12 m to 60 m, which helps explain the behaviour of the deviations of the elevation estimates of the second target over this range.

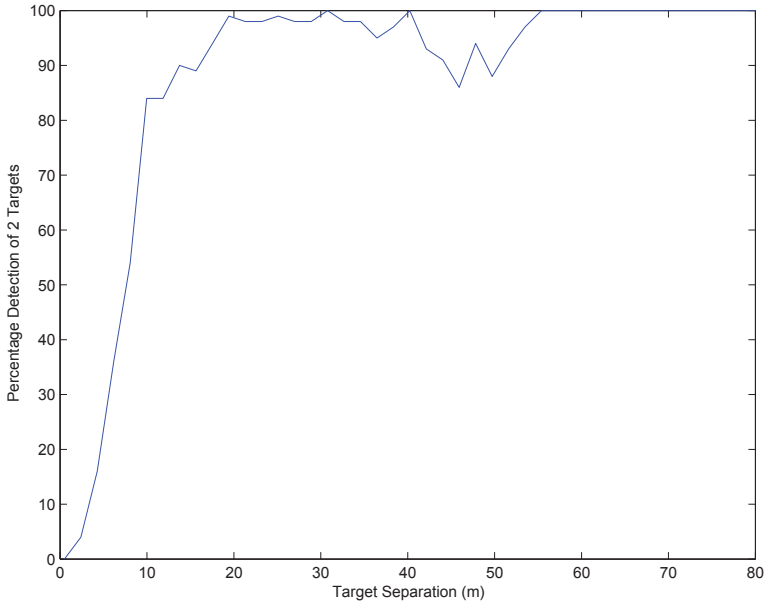

Figure 34: *Probability of detection of two distinct targets as a function of the target separation in Geometry 1. The SNR of both targets is 5 dB.*

4.4 Simulation for Geometry 2 with two targets

The simulations to investigate the ability of the CS approach to resolve two targets were also conducted for Geometry 2. Due to the smaller synthetic aperture and increased range in this geometry (see Table 2), the performance of the deviation of elevation estimates is expected to be worse than in Geometry 1. Figure 35 shows the mean of the elevation estimates of the two targets when the SNR is 20 dB. In this case, the estimates appear to be unbiased at target separations less than 10 m and greater than 45 m. The estimates display more significant bias between 10 m and 45 m. Even at this high SNR the CS approach does not perform well unless the targets are well separated.

Figure 36 displays the standard deviations of the elevation estimates for the two targets, when the SNR is 20 dB. Figure 37 shows the corresponding detection performance for detecting two distinct targets as a function of their separation distance. Two distinct targets are detected until the separation becomes less than 30 m. When

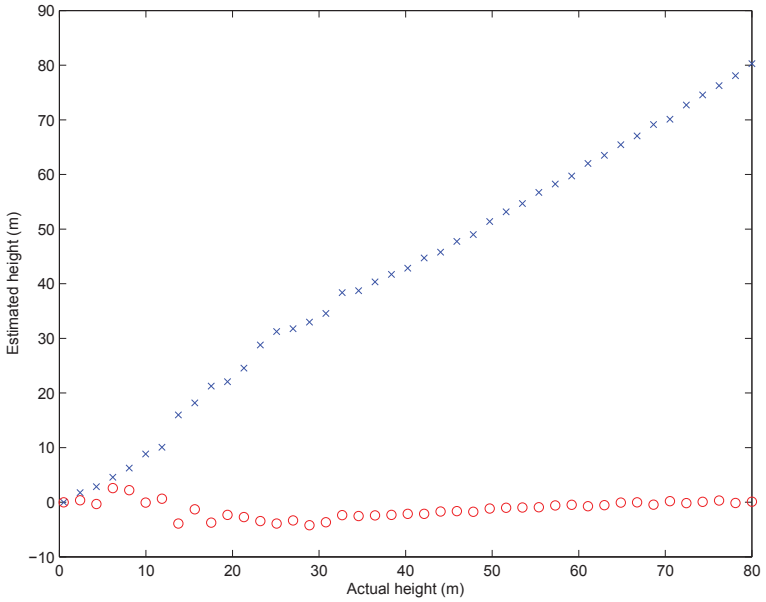

Figure 35: *Mean of estimated heights for two targets in Geometry 2. The SNR for both targets is 20 dB. The elevations are plotted as a function of the true height of the target with the varying elevation.*

the target separation is greater than 30 m, the deviations of the elevation estimate are less than 7m. When the target separation is less than 30 m, the deviations of the elevation estimates of both targets increase. The deviations of the estimates begin to drop once the target separation is less than 15 m.

Figure 38 shows the mean of the elevation estimates of the two targets when the SNR is 10 dB. In this case, the estimates appear to be unbiased at target separations less than 10 m and greater than 45 m. Figure 39 displays the standard deviations of the elevation estimates for the two targets, when the SNR is 10 dB. Figure 40 shows the corresponding detection performance for detecting two distinct targets as a function of their separation distance. The behaviour of the deviations of the elevation estimates is similar to when the SNR is 20 dB. The deviations of the estimates peak over the 10 m–40 m elevation range, which corresponds to where the algorithm has difficultly detecting two distinct targets. At separations greater than 40 m, the deviation of the estimates is less than 10 m, which corresponds to when the algorithm consistently detects two distinct targets.

Figure 41 shows the mean of the elevation estimates of the two targets when the SNR is 5 dB. In this scenario, the estimates generally appear unbiased, but there are some small variations about the true values. Figure 42 shows the corresponding deviations of the elevation estimates. The non-uniform behaviour of the deviations of the estimates is readily apparent. The largest deviation appears when the targets

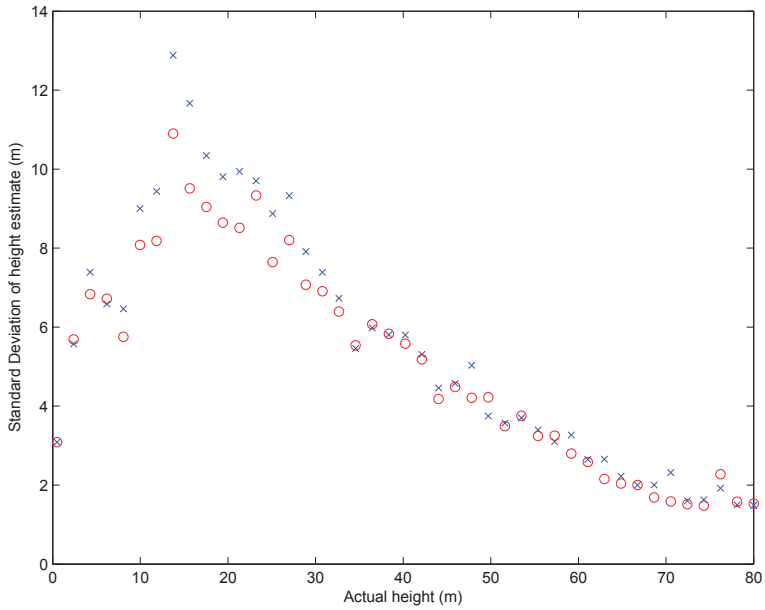

Figure 36: *Standard deviation of estimated heights for two targets in Geometry 2. The SNR for both targets is 20 dB. The deviations are plotted as a function of the true height of the target with the varying elevation.*

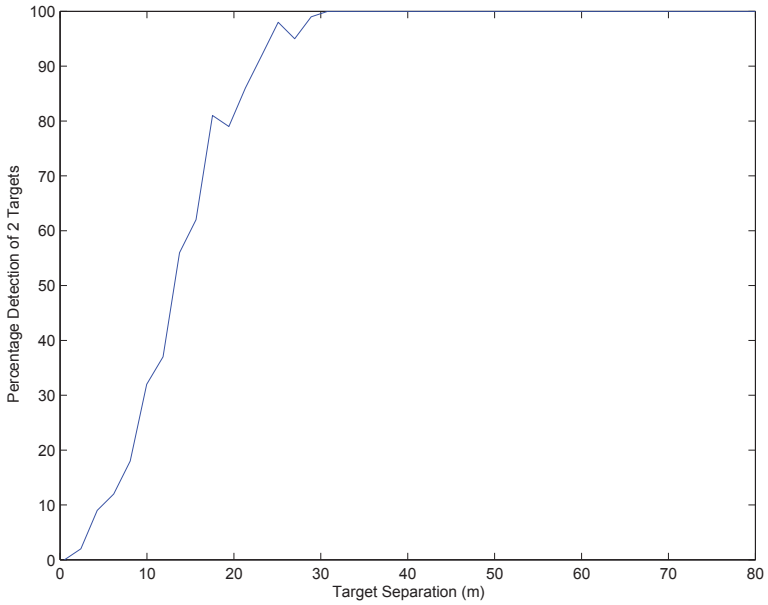

Figure 37: *Probability of detection of two distinct targets as a function of the target separation in Geometry 2. The SNR of both targets is 20 dB.*

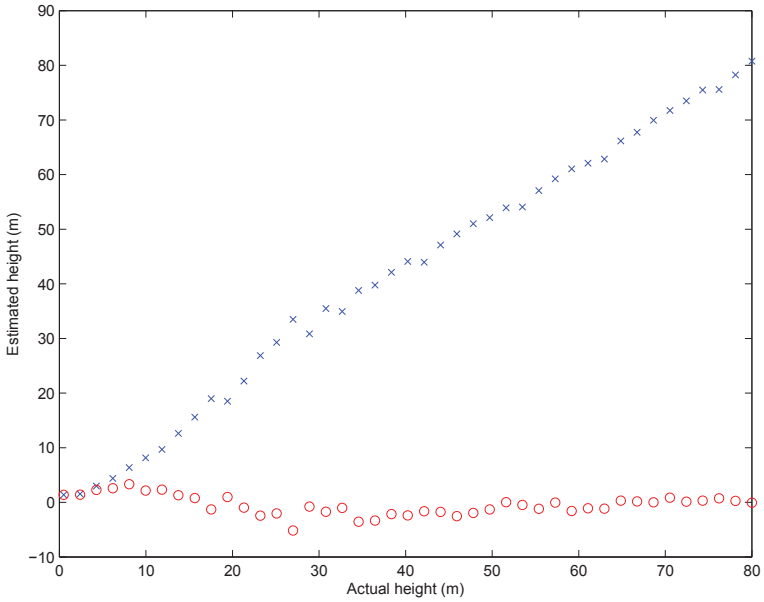

Figure 38: *Mean of estimated heights for two targets in Geometry 2. The SNR for both targets is 10 dB. The elevations are plotted as a function of the true height of the target with the varying elevation.*

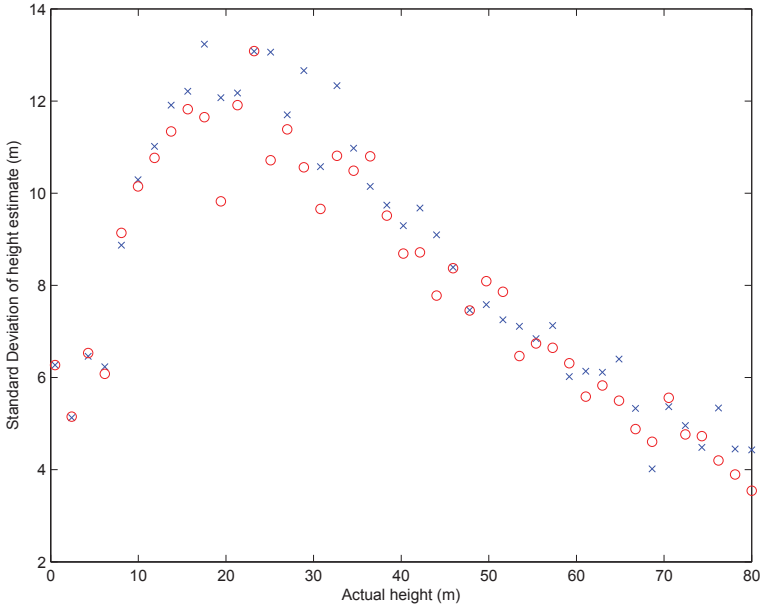

Figure 39: *Standard deviation of estimated heights for two targets in Geometry 2. The SNR for both targets is 10 dB. The deviations are plotted as a function of the true height of the target with the varying elevation.*

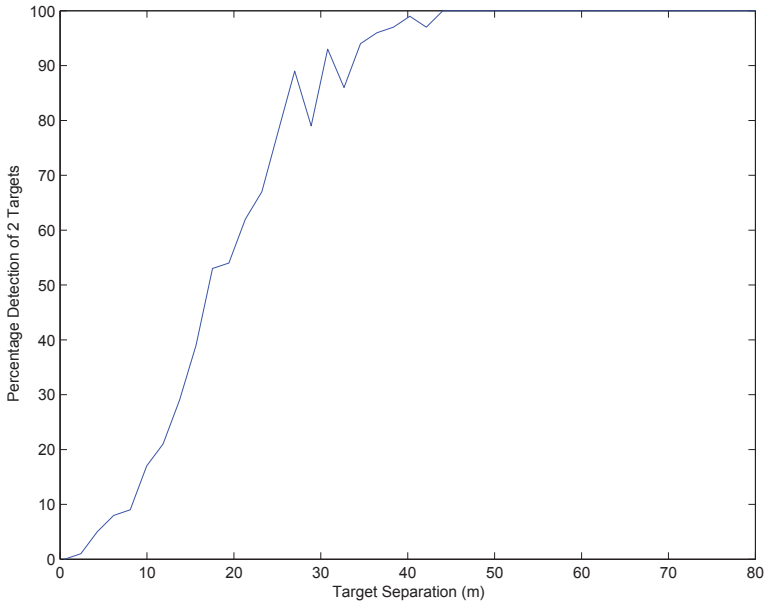

Figure 40: *Probability of detection of two distinct targets as a function of the target separation in Geometry 2. The SNR of both targets is 10 dB.*

are approximately separated by 30 m. Figure 43 shows the corresponding detection performance of detecting two distinct targets. At 5 dB SNR, the algorithm only consistently detects two distinct targets when their separation is greater than 60 m.

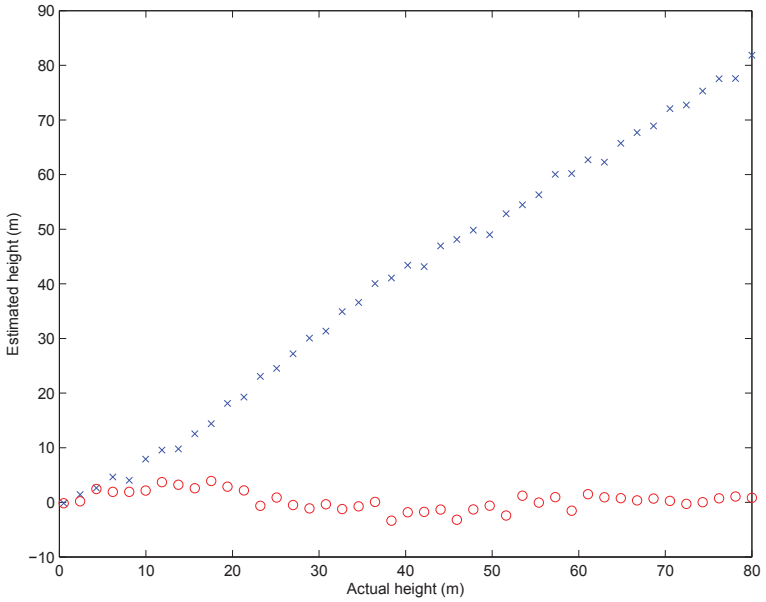

Figure 41: *Mean of estimated heights for two targets in Geometry 2. The SNR for both targets is 5 dB. The elevations are plotted as a function of the true height of the target with the varying elevation.*

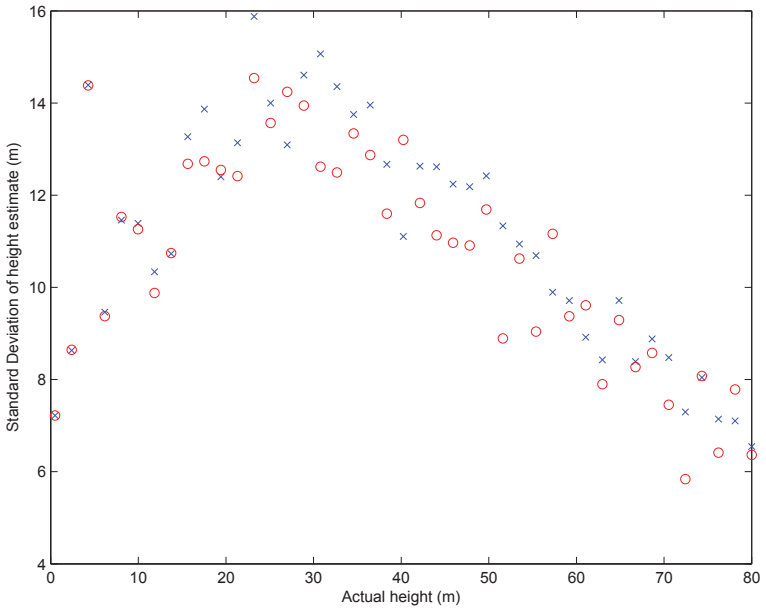

Figure 42: *Standard deviation of estimated heights for two targets in Geometry 2. The SNR for both targets is 5 dB. The deviations are plotted as a function of the true height of the target with the varying elevation.*

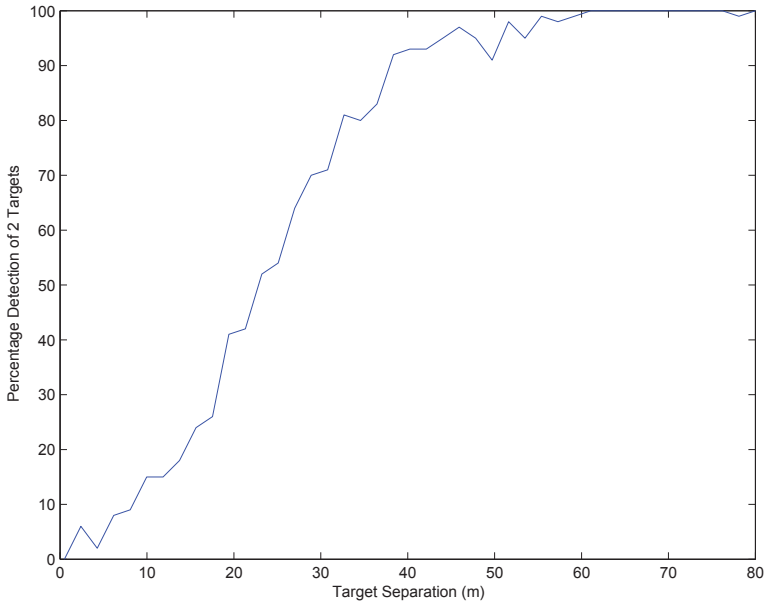

Figure 43: *Probability of detection of two distinct targets as a function of the target separation in Geometry 2. The SNR of both targets is 5 dB.*

4.5 Simulations for Geometry 3 with one target

In the previous simulations eight satellite passes were used for the tomographic processing. In the configuration for Geometry 3 a total of 31 satellite passes are used. The 31 passes include the original eight passes from Geometry 1 and an additional 23 randomly generated passes. These passes are more representative of the data that could be collected under the RADARSAT Constellation Mission where the interval between coherent data collections would be shorter. The simulations in this section utilize a single target at various elevations. Figure 44 shows the mean estimates of the target elevation as a function of the true target elevation for SNR=20 dB. The mean values correspond very well with the true target elevations. Figure 45 shows the corresponding standard deviations of the elevation estimates as a function of the true elevation. The deviations are uniformly distributed between 0.3 m and 0.46 m across all target elevation values. Comparison of the deviations with those in Figure 13 reveals that the increased number of satellite passes and increased aperture length results in lower deviations of the elevation estimates.

Figure 46 shows the mean estimates of the target elevation as a function of the true target elevation for SNR=10 dB. The mean values correspond very well with the true target elevations. Figure 47 shows the corresponding standard deviations of the elevation estimates as a function of the true elevation. The deviations are uniformly distributed between 0.75 m and 1.1 m across almost all the target elevation values. Near the 52 m elevation point, the deviation of the estimate jumps to 4.8 m. Other

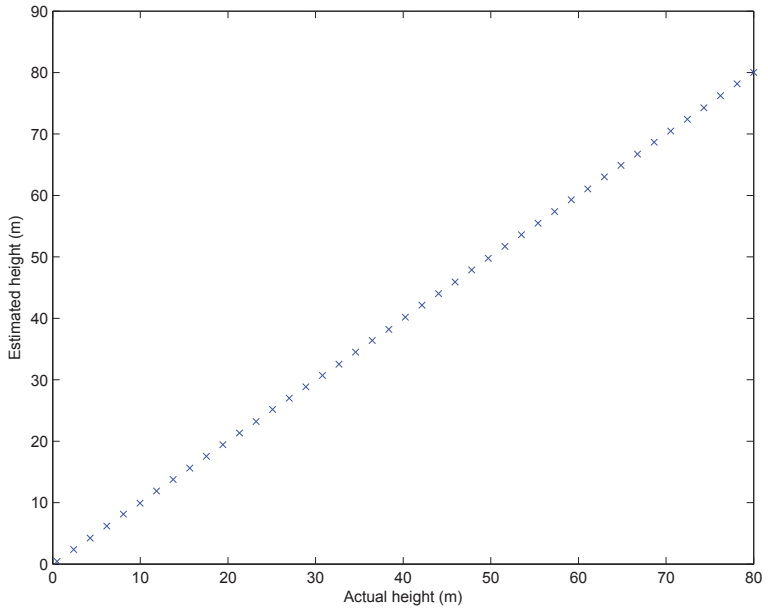

Figure 44: *Mean of estimated height vs. true height for a single target for Geometry 3. SNR=20 dB.*

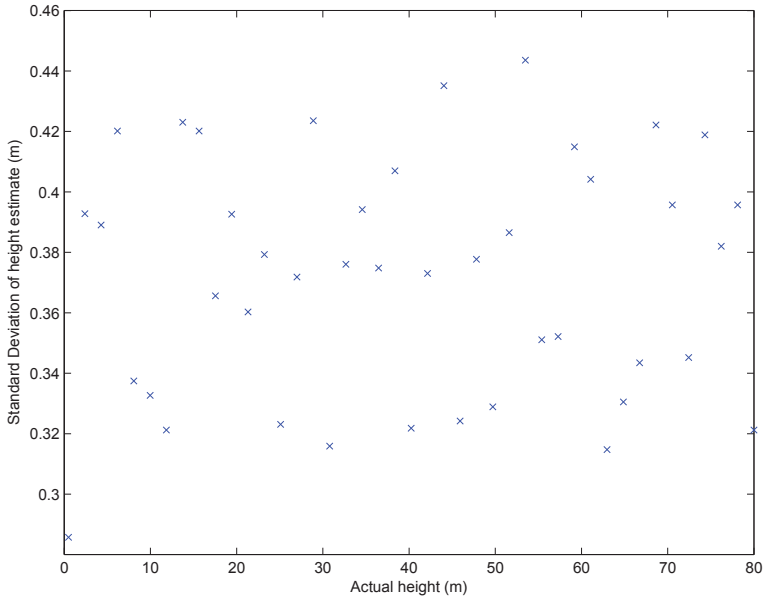

Figure 45: *Standard deviation of the estimated height vs. the true height for Geometry 3. SNR=20 dB.*

than the anomaly at m, the deviations of the estimates are very similar to the deviations of the estimates in Geometry 1 at SNR=10 dB.

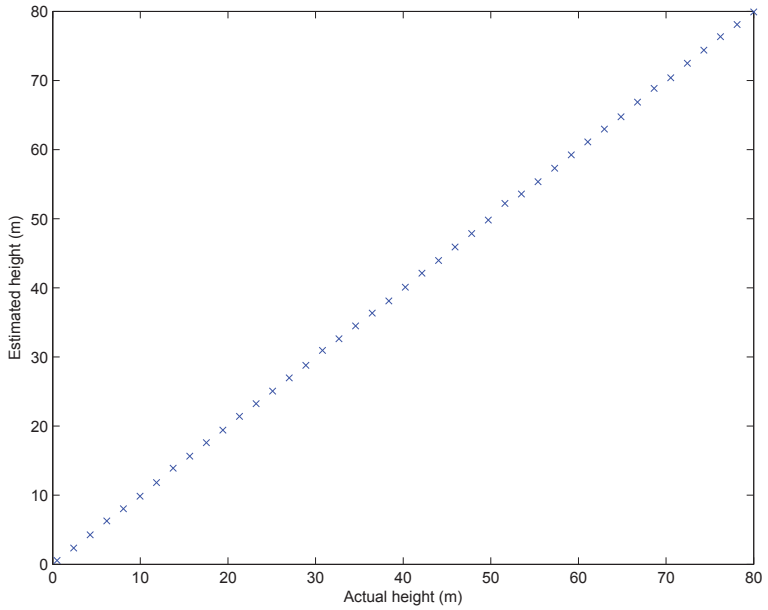

Figure 46: *Mean of estimated height vs. true height for a single target for Geometry 3. SNR=10 dB.*

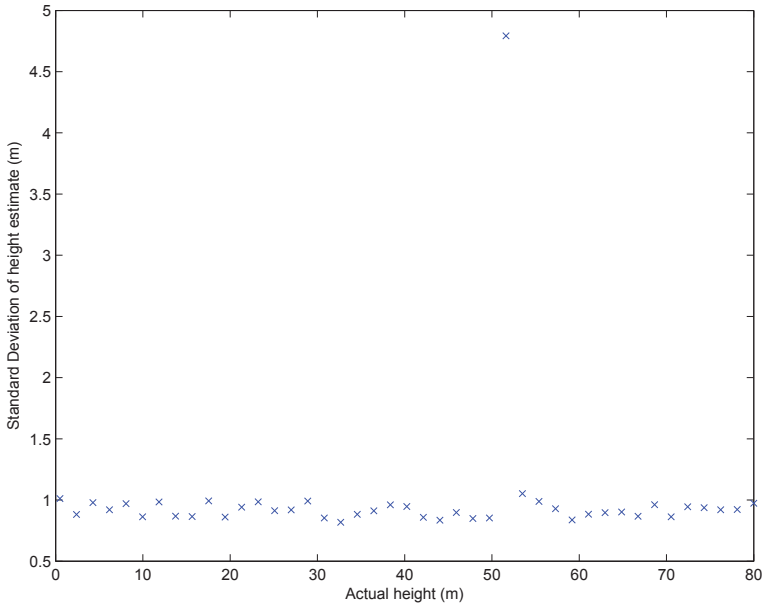

Figure 47: *Standard deviation of the estimated height vs. the true height for Geometry 3. SNR=10 dB.*

Figure 48 shows the mean estimates of the target elevation as a function of the true target elevation for SNR=5 dB. The mean values correspond very well with the true

target elevations. A small bias begins to appear in the estimates for target elevations between 40 m and 60 m. Figure 49 shows the corresponding standard deviations of the elevation estimates as a function of the true elevation. Across most of the target elevations, the deviations of the estimates are less than 2 m. Over the target elevation range of 40 m to 60 m, the deviations of the estimates increase up to 7.5 m and increased deviations are also seen in the 20 m to 30 m elevation range. Comparing Figure 49 and Figure 17 reveals that the increased number of measurements and increased aperture has not resulted in a significant improvement of the deviations of the elevation estimates at this SNR.

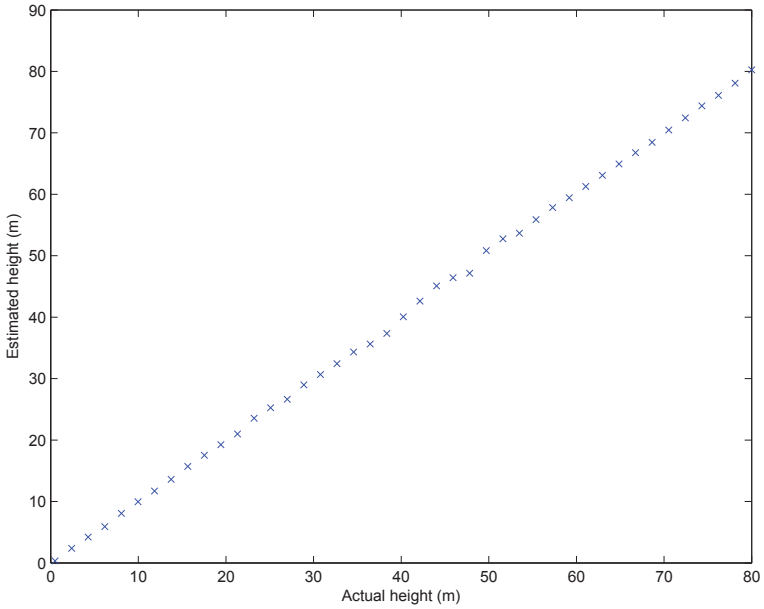

Figure 48: *Mean of estimated height vs. true height for a single target for Geometry 3. SNR=5 dB.*

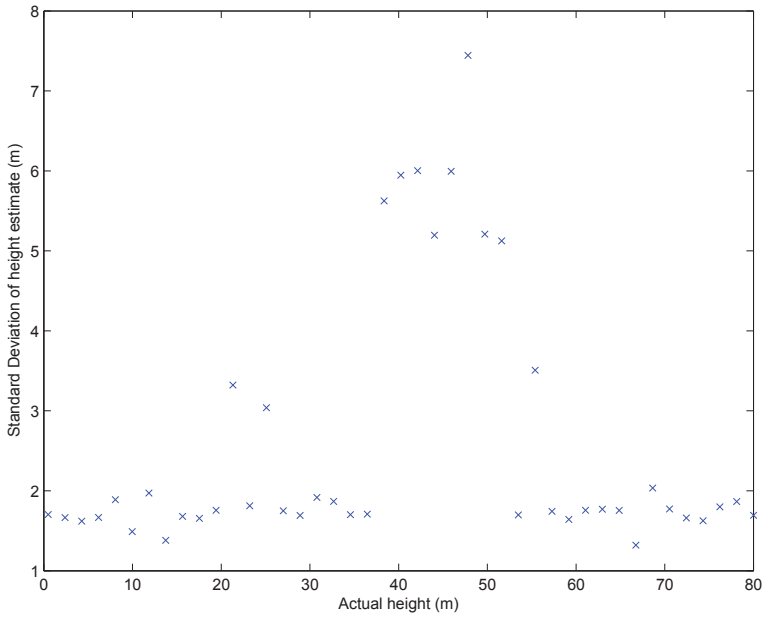

Figure 49: *Standard deviation of the estimated height vs. the true height for Geometry 3. SNR=5 dB.*

4.6 Simulations for Geometry 3 with two targets

In the previous section we saw that the increased number of measurements and the increase aperture lead to improved estimation of the elevation for a single target at various SNRs. In this section, the estimation performance on two targets is presented for the configuration in Geometry 3. Figure 50 shows the mean value of the elevation estimates of the two targets when their SNR is 20 dB. For the majority of the target elevation values the mean estimates correspond well with their true values. Near 50 m elevation the estimates display a more significant bias. Given the behaviour displayed with the same geometry for a single target at both 10 dB and 5 dB, it is expected that the performance of the deviation of the elevation estimates in the range 40 m to m will be poor.

Figure 51 shows the standard deviations of the estimates for the two targets in Geometry 3 when the SNR is 20 dB. Over the most of the target elevations, the deviations of both estimates are less 4 m. Over the range 40 m to 60 m, the deviations of the elevation estimates for the elevated target increase to just over 13 m. The deviations of estimates for the target at 0 m elevation also increase over this range, but remain less than 2 m. The deviations for both targets gradually increase as the targets move from a 20 m separation to a 5 m separation. Examining of the detection performance in Figure 52 indicates that the increase in the deviations is likely due to the inability of the algorithm to consistently detect two targets across this elevation range. Further examination of the detection performance reveals that the algorithm has difficultly

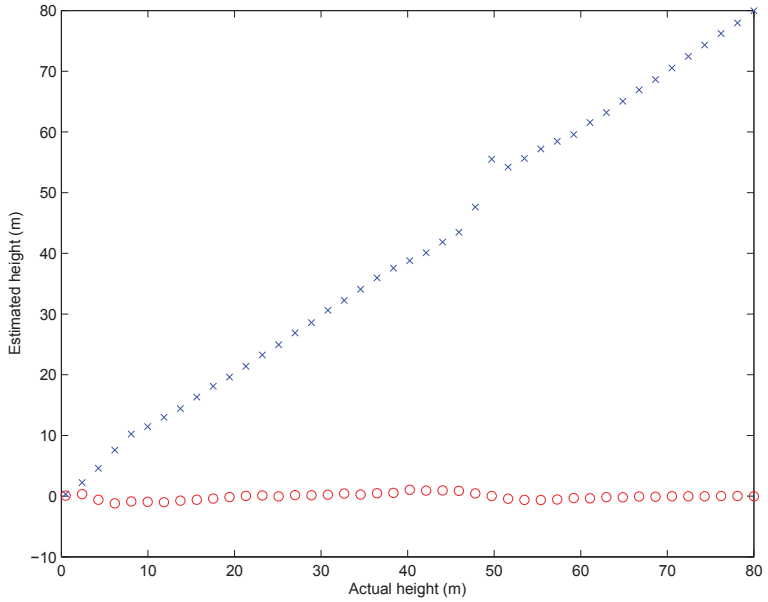

Figure 50: *Mean of estimated heights for two targets in Geometry 3. The SNR for both targets is 20 dB. The elevations are plotted as a function of the true height of the target with the varying elevation.*

detecting two distinct targets at the 50 m elevation.

Figure 53 shows the mean value of the elevation estimates of the two targets when their SNR is 10 dB. For the majority of the target elevation values, the mean estimates correspond well with the true values. Near 50 m elevation the estimates display more pronounced biasing than with the higher SNR scenarios. Additionally, the mean values display some bias when the targets are quite close together. Figure 54 shows the deviations of the target elevation estimates. The general behaviour of the deviations is similar to that of the SNR=20 dB scenario, but the deviations have increased at the lower SNR. It should also be noticed that when the target separation is small, the deviations of the estimates exhibit a sharp increase. This increase is likely due to the biased nature of the estimates at these elevations.

Figure 55 shows the detection performance for detecting two distinct targets for this geometry when the SNR is 10 dB. At this SNR the algorithm is not able to consistently detect two targets as their separation falls below 20 m. The algorithm also has difficultly separating two distinct targets when the second target is within the 40 m to 55 m elevation range.

Figure 56 shows the mean value of the elevation estimates of the two targets when their SNR is 5 dB. The mean estimates display more variability across the elevation range than was seen at the higher SNRs. Near 50 m, the mean estimate of the elevated target is less biased than at the 10 dB SNR, while the estimate for target at 0 m

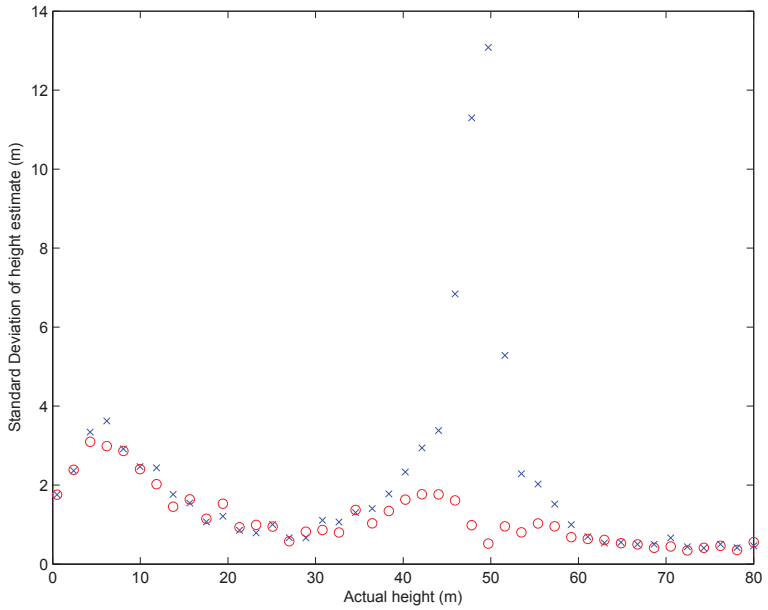

Figure 51: *Standard deviation of estimated heights for two targets in Geometry 3. The SNR for both targets is 20 dB. The deviations are plotted as a function of the true height of the target with the varying elevation.*

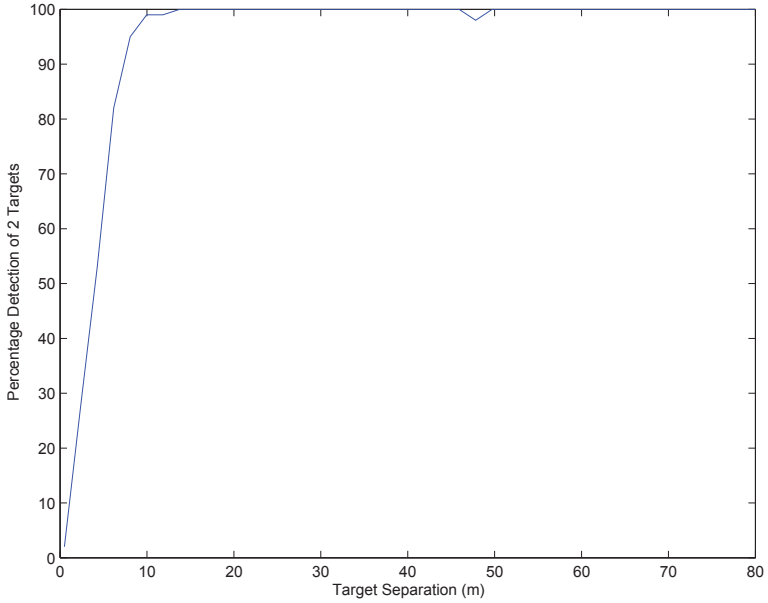

Figure 52: *Probability of detection of two distinct targets as a function of the target separation in Geometry 3. The SNR of both targets is 20 dB.*

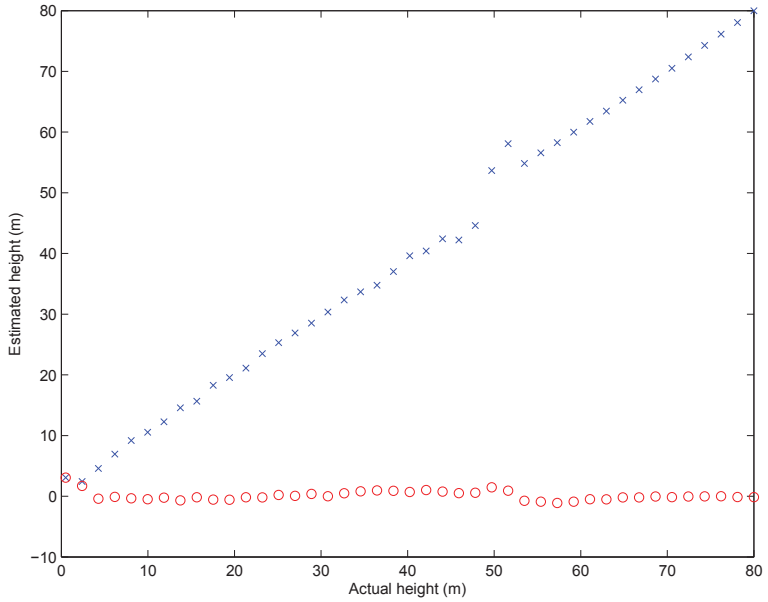

Figure 53: *Mean of estimated heights for two targets in Geometry 3. The SNR for both targets is 10 dB. The elevations are plotted as a function of the true height of the target with the varying elevation.*

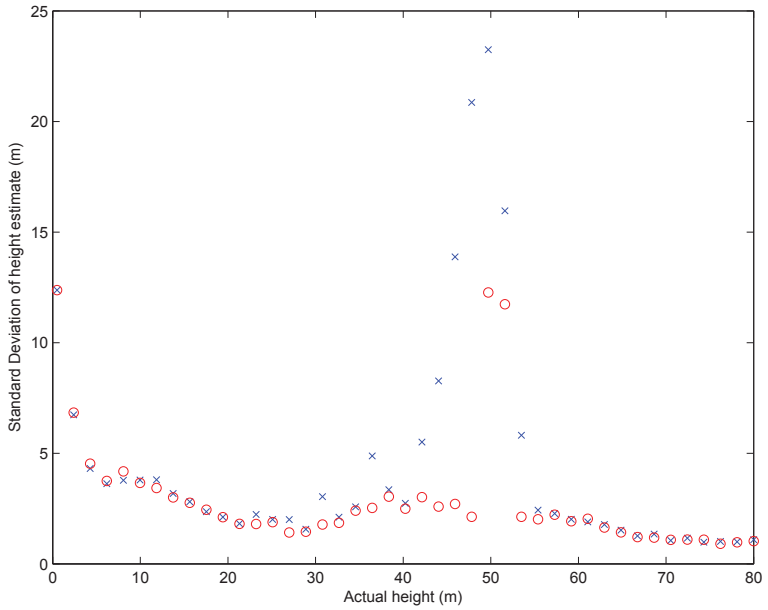

Figure 54: *Standard deviation of estimated heights for two targets in Geometry 3. The SNR for both targets is 10 dB. The deviations are plotted as a function of the true height of the target with the varying elevation.*

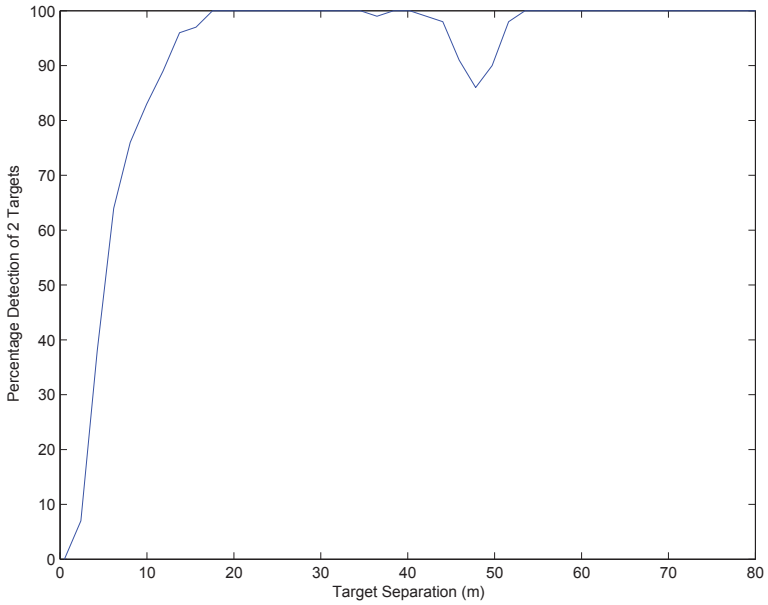

Figure 55: *Probability of detection of two distinct targets as a function of the target separation in Geometry 3. The SNR of both targets is 10 dB.*

elevation appears to be more biased than was seen at 10 dB SNR. Figure 57 shows the deviations of the target elevation estimates. The behaviour of the deviations for both targets is quite similar. The deviations range from 1.8 m to 22 m. The peak deviations occur when the targets are close together and when the elevated target is in the 40 m to 60 m elevation range.

Figure 58 shows the probability of detecting two distinct targets for this geometry when the SNR is 5 dB. At this SNR the algorithm is not able to consistently detect two targets for separations less than 60 m. There is also a drop in the detection performance for the target elevation range between 40 m and 60 m, which is consistent with the trend seen at higher signal to noise ratios.

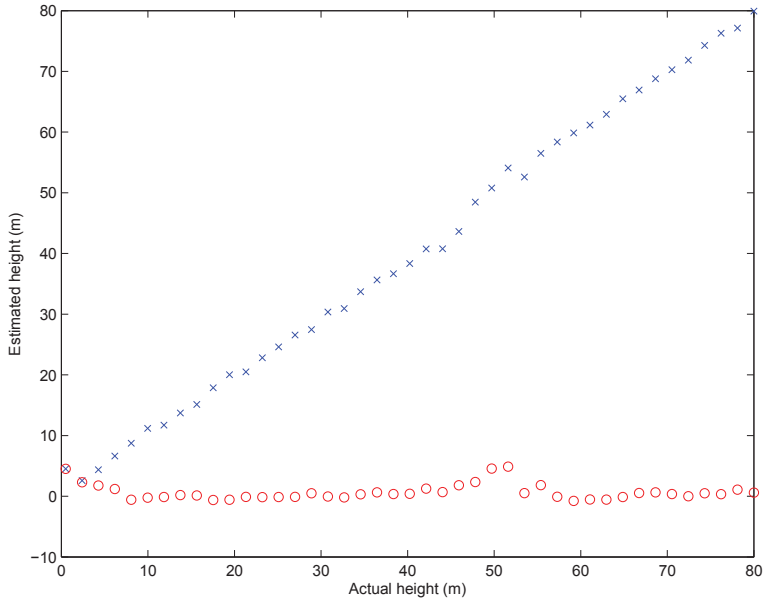

Figure 56: *Mean of estimated heights for two targets in Geometry 3. The SNR for both targets is 5 dB. The elevations are plotted as a function of the true height of the target with the varying elevation.*

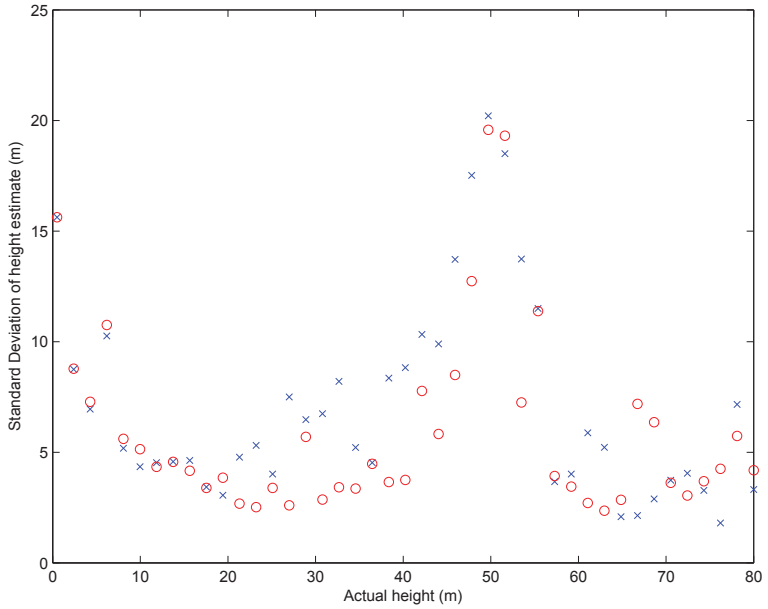

Figure 57: *Standard deviation of estimated heights for two targets in Geometry 3. The SNR for both targets is 5 dB. The deviations are plotted as a function of the true height of the target with the varying elevation.*

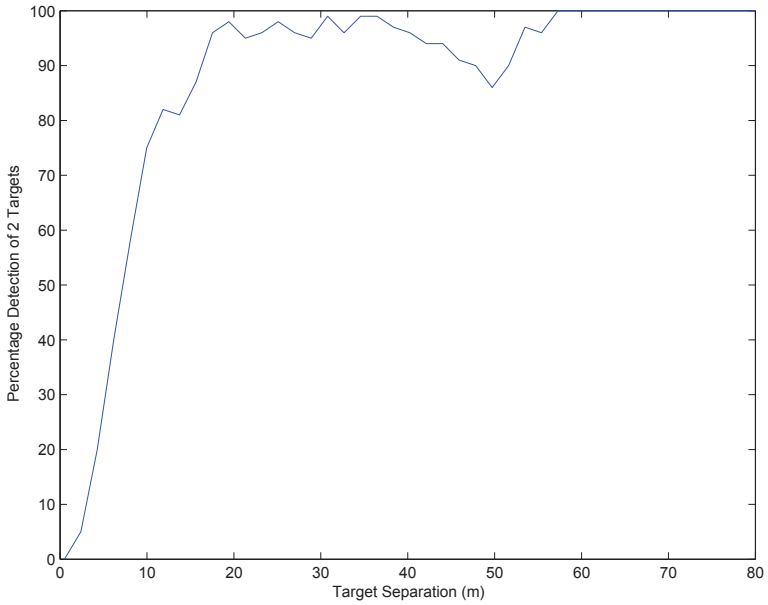

Figure 58: *Probability of detection of two distinct targets as a function of the target separation in Geometry 3. The SNR of both targets is 5 dB.*

4.7 Simulations for Geometry 4 with two targets

Geometry 4 is essentially the same as Geometry 2, except that 31 orbital measurements are used. The 31 orbits include the eight orbits from Geometry 2 and an additional 23 randomly generated orbits. In Section 4.5 the performance improvement of the Compressive Sensing algorithm with the additional measurements in Geometry 3 for a single target were compared against Geometry 1. Geometry 4 is expected to behave in a similar fashion; therefore the simulations with a single target in Geometry 4 were not conducted. It is of interest to discover if the additional measurements result in a significant improvement of the elevation estimation performance over Geometry 2 when two targets are present.

Figure 59 shows the mean value of the elevation estimates for two targets when the SNR is 20 dB. The estimates appear to be consistent over the elevation range 35 m to 80 m, but display some bias when the elevated target is less than 35 m. Figure 60 shows the standard deviations of the elevation estimates for the two targets as a function of the elevated target's height. The deviations for both targets follow the same pattern. When the elevated target is at 80 m, the deviations of the estimates are less than 2 m. As the elevated target is moved closer to the other target at 0 m, the deviations of the estimates increase until they reach a maximum value of 12 m at the 12 m elevation. When the targets are less than 12 m apart, the deviations of the estimates begin to decrease.

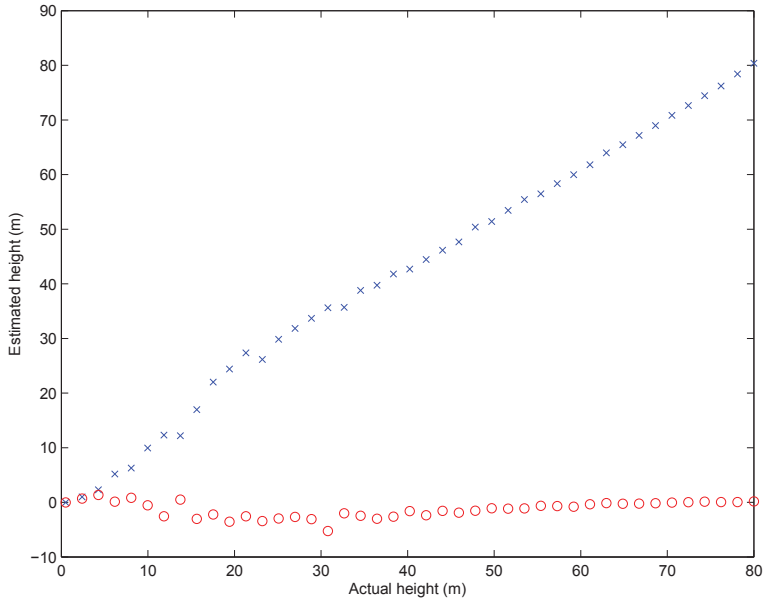

Figure 59: *Mean of estimated heights for two targets in Geometry 4. The SNR for both targets is 20 dB. The elevations are plotted as a function of the true height of the target with the varying elevation.*

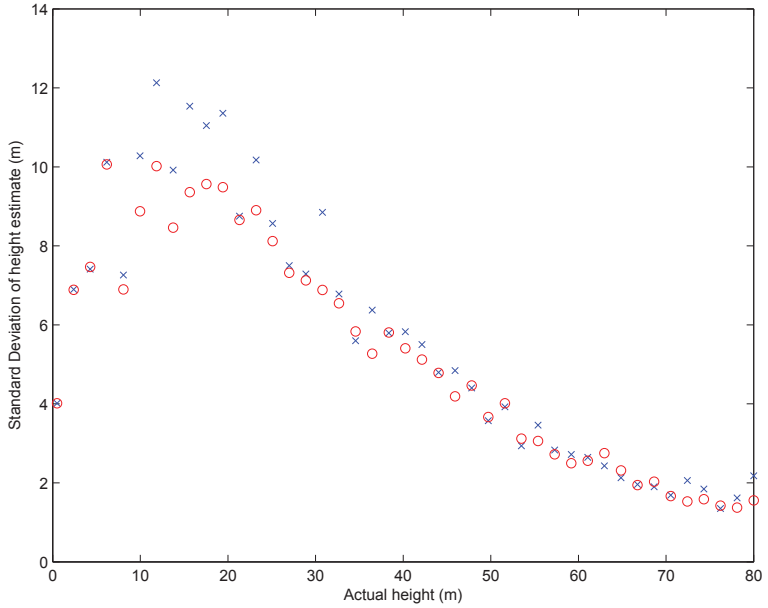

Figure 60: *Standard deviation of estimated heights for two targets in Geometry 4. The SNR for both targets is 20 dB. The deviations are plotted as a function of the true height of the target with the varying elevation.*

Figure 61 shows the corresponding detection performance for detecting two distinct targets as a function of their separation distance. The algorithm consistently detects two separate targets when then separation is greater than 35 m. The detection of only a single target below this elevation and the bias of the estimates lead to the increased deviation of the estimates until the targets are sufficiently close together.

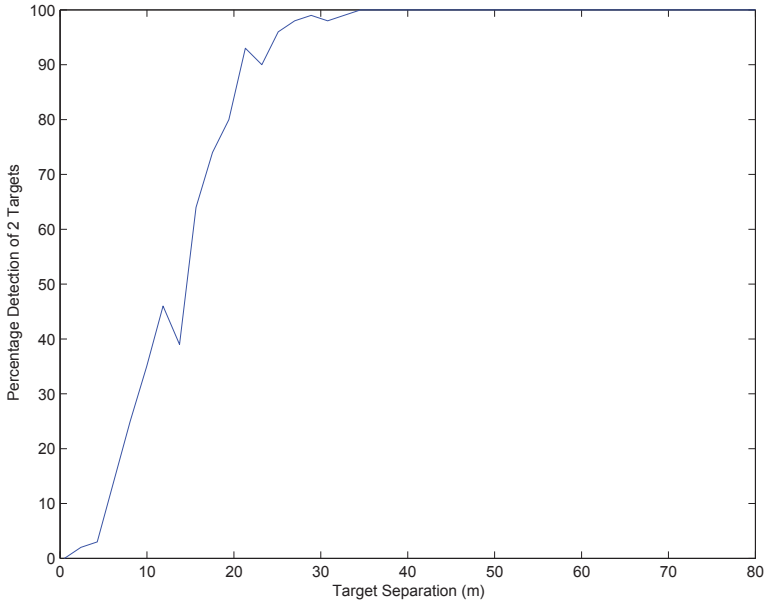

Figure 61: *Probability of detection of two distinct targets as a function of the target separation in Geometry 3. The SNR of both targets is 20 dB.*

Figure 62 shows the mean value of the elevation estimates of the two targets when their SNR is 10 dB. The estimates appear to be consistent over the elevation range 40 m to 80 m, but some estimation bias appears when the elevated target is less than 40 m in elevation. Figure 63 shows the standard deviations of the elevation estimates for the two targets as a function of the elevated target's height. The deviations for both targets follow the same pattern. When the elevated target is at 80 m, the deviations of the estimates are less than 4 m. As the elevated target is moved closer to the other target, the deviations of the estimates increase until they peak at a value of 15 m when the elevated target is at 22 m elevation. When the targets are less than 22 m apart, the deviations of the estimates begin to decrease.

Figure 64 shows the probability of detection of two distinct targets as a function of the target separation distance when the SNR is 10 dB. The algorithm is only able to consistently detect two separate targets when their separation is greater than 50 m. Below this elevation, the detection performance degrades rapidly as the targets move closer together. The algorithm is able to detect two distinct targets better than 80% of the time when the separation distance is larger than 28 m.

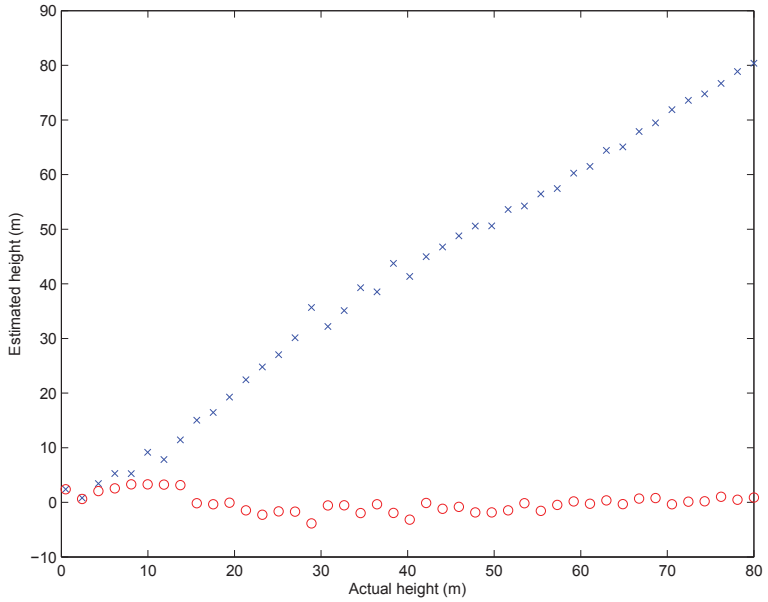

Figure 62: *Mean of estimated heights for two targets in Geometry 4. The SNR for both targets is 10 dB. The elevations are plotted as a function of the true height of the target with the varying elevation.*

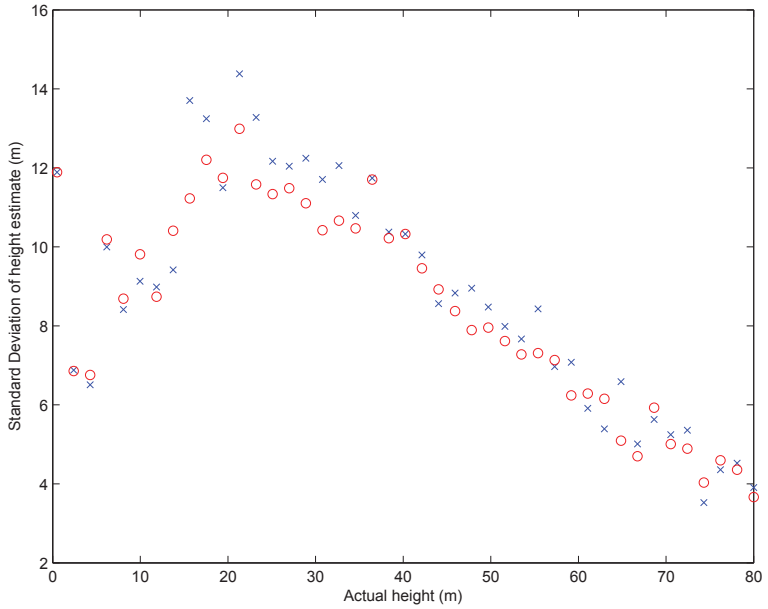

Figure 63: *Standard deviation of estimated heights for two targets in Geometry 3. The SNR for both targets is 10 dB. The deviations are plotted as a function of the true height of the target with the varying elevation.*

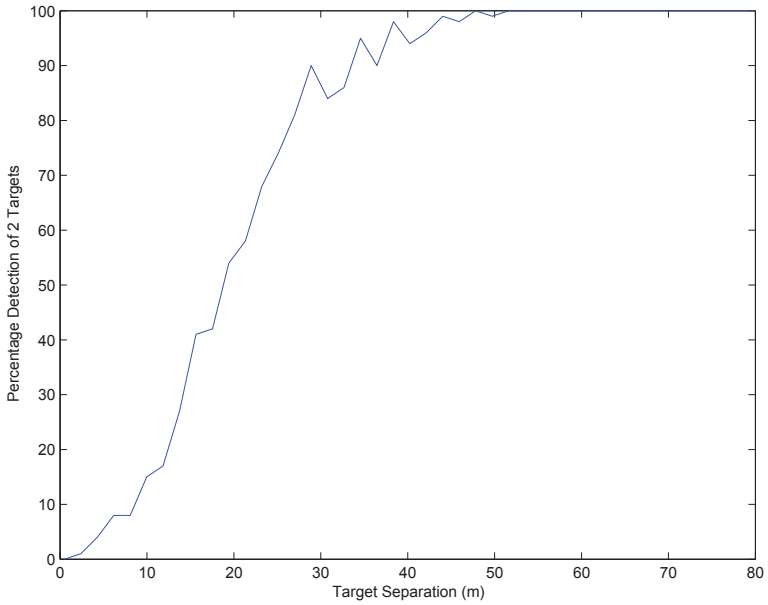

Figure 64: *Probability of detection of two distinct targets as a function of the target separation in Geometry 4. The SNR of both targets is 10 dB.*

Figure 65 shows the mean value of the elevation estimates of the two targets when their SNR is 5 dB. There are small discrepancies in the mean estimates for the target elevation range between 25 m and 70 m. A larger bias in the estimates occurs when the target elevation is less than 25 m. Figure 66 shows the corresponding standard deviations of the elevation estimates for the two targets as a function of the elevated target's height. The deviations for both targets follow the same pattern. When the elevated target is at 80 m the deviations of the estimates are less than 10 m. As the elevated target is moved closer to the other target, the deviations of the estimates increase until they peak at a value of 15.5 m when the elevated target is at 22 m elevation. When the targets are less than 22 m apart, the deviations of the estimates begin to decrease. Over the target elevation range from 40 m to 80 m, the deviations of elevation estimates are higher at the SNR=5 dB than when the SNR=10 dB. For the elevation range below 40 m, the deviations of the estimates for SNR=5 dB are only slightly higher than when the SNR=10 dB.

Figure 67 shows the probability of detection of two distinct targets as a function of the target separation distance when the SNR is 5 dB. The algorithm is only able to consistently detect two distinct targets when their separation is greater than 60 m. Even at these separations there are elevations where the performance dips below 100 percent.

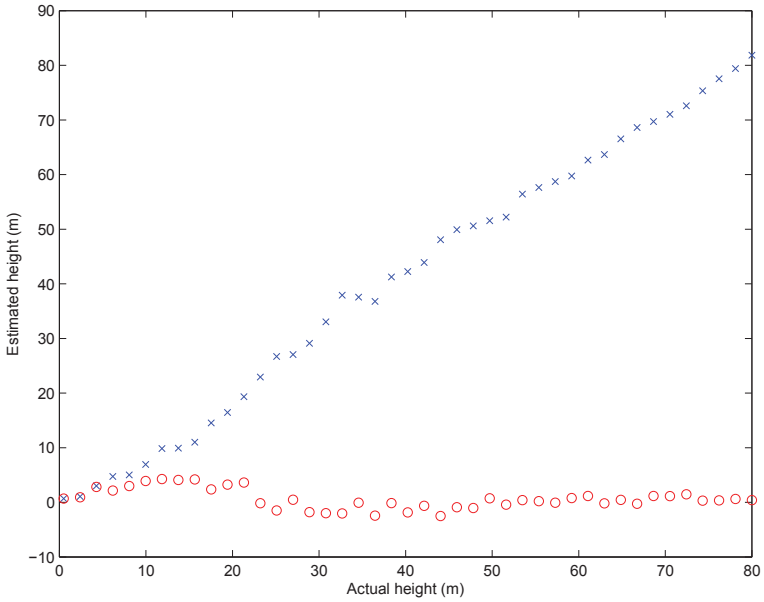

Figure 65: *Mean of estimated heights for two targets in Geometry 4. The SNR for both targets is 5 dB. The elevations are plotted as a function of the true height of the target with the varying elevation.*

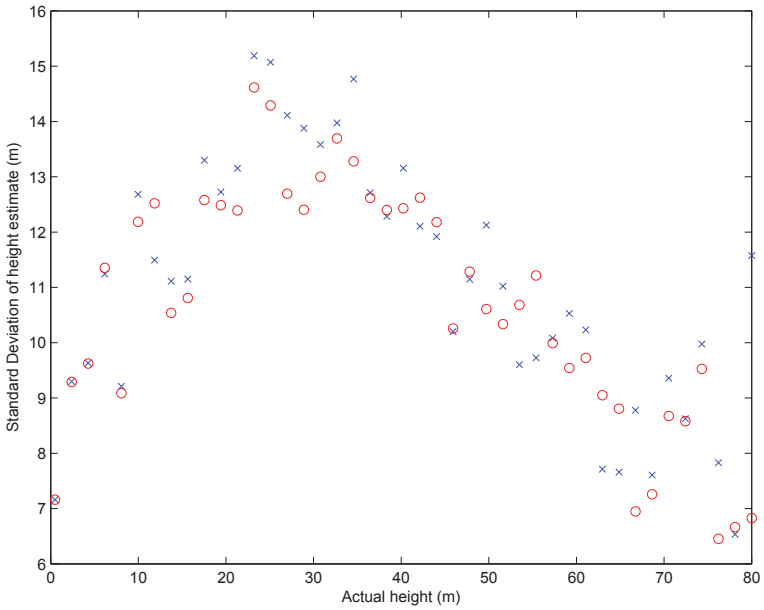

Figure 66: *Standard deviation of estimated heights for two targets in Geometry 4. The SNR for both targets is 5 dB. The deviations are plotted as a function of the true height of the target with the varying elevation.*

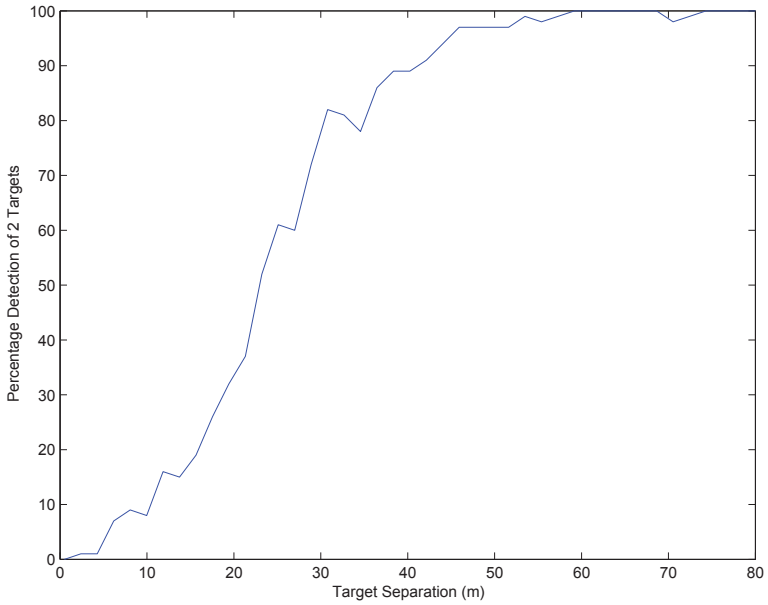

Figure 67: *Probability of detection of two distinct targets as a function of the target separation in Geometry 4. The SNR of both targets is 5 dB.*

5 Conclusions

In the case of a single target and a small number of measurements the CS approach for target elevation estimation works well across the range of geometries and SNRs investigated. As the SNR decreases, the standard deviation of the estimates generally increases. It also appears that the discretization of the problem space also affects the performance of the estimates. In the case of Geometry 1 at SNR=5 dB, the standard deviation of the estimates is dependent on the height of the actual target, while for Geometry 2 at the same SNR the standard deviation remains fairly constant across all the target elevations. This result is not completely unexpected since much of the theory surrounding compressive sensing pertains to the RIP constant, or similar measures, which constrain how closely the vectors in the columns of the matrix $\mathbf{A}$ are spaced in the elevation grid. Even when the number of measurements is increased to 31 the behaviour of the both the mean and standard deviation of the estimates remains essentially unchanged from the results for the geometry with fewer measurements.

In the case of two targets separated in elevation the performance of the mean of the elevation estimates are generally consistent, but a small bias does appear at some elevation estimates. The bias tends to become more pronounced as the SNR decreases, but even at high SNRs there are certain target elevations which display more bias in their estimates. The elevations that are biased are the same elevations that have larger deviations in the single target case. This behaviour is likely due to the discretization of the elevation space.

The standard deviation of the elevation estimates in the case of two targets is larger than that in the single target case. The deviation of the elevation estimates of the target that is located on the discretization grid is generally better than the deviation of the elevation estimates of the target not on the grid. As the SNR decreases, the standard deviation of the target elevation estimates increases. Also, the ability of the algorithm to correctly detect two distinct targets, when they are closely spaced together, degrades significantly as the SNR decreases from 20 dB to 5 dB.

When the number of measurements is increased to 31, the mean and standard deviation of the estimates in the two target case remain almost unchanged from the eight measurement case. The increased number of measurements does provide a slight improvement in the algorithms ability to detect two distinct targets that are closely spaced together.

These results indicate the CS approach to multi-pass satellite tomography is a viable approach; however, it should be reserved for use in SAR resolution cells that have high SNRs and where there is strong coherence in the dominant scatterers across the multiple measurements. Therefore, pre-processing of the SAR images should be performed to choose the appropriate resolution cells for tomographic processing. Since

many of the compressive sensing algorithms are iterative, this will reduce the overall computational complexity of forming a tomographic image. In these simulations the number of targets is assumed to be known, which is not the case in practice. When the number of targets is known it is fairly straightforward to choose the value of the parameter in the CS algorithm. Algorithms for choosing the appropriate values of these parameters when the number of targets is unknown are a topic of active research.

From the results of the simulations it is also apparent that the discretization grid affects the performance of the CS algorithms. Comparing the deviation of the elevation estimates for Geometry 1 and Geometry 2 at SNR=5 dB shows that while Geometry 1 has lower deviations for most target elevations there are certain elevations that produce larger deviations. For Geometry 2, the deviations of the elevation estimates are consistent across the range of target elevations. Due to the nature of compressive sensing, the process can be repeated for a different discretization of the sample space. An active area of research is investigating methods of adjusting the vectors in the $\mathbf{A}$ matrix to account for modeling errors. Some of these methods include: resampling the grid [47, 48], Total Least Squares [43], and gridless methods [49, 50, 51]. These methods are currently an area of active research in compressive sensing algorithms.

This page intentionally left blank.

References

[1] Richards, J. A. (2009), Remote Sensing with Imaging Radar, Springer.

[2] Hanssen, R. F. (2001), Radar interferometry: Data interpretation and error analysis, Remote Sensing and Digital Image Processing, Kluwer Academic Publishers.

[3] Zhu, X. X., and Bamler, R. (2011), Let's Do the Time Warp: Multicomponent Nonlinear Motion Estimation in Differential SAR Tomography, *IEEE Geoscience and Remote Sensing Letters*, 8(4), 735–739.

[4] Soumekh, M. (1999), Synthetic Aperture Radar Signal Processing with MATLAB Algorithms, 1 edition ed, New York: Wiley-Interscience.

[5] Pasquali, P., Prati, C., Rocca, F., Seymour, M., Fortuny, J., Ohlmer, E., and Sieber, A. (1995), A 3-D SAR experiment with EMSL data, In *Geoscience and Remote Sensing Symposium, 1995. IGARSS '95. 'Quantitative Remote Sensing for Science and Applications', International*, Vol. 1, pp. 784–786.

[6] Fornaro, G., and Pauciullo, A. (2009), LMMSE 3-D SAR Focusing, *IEEE Transactions on Geoscience and Remote Sensing*, 47(1), 214–223.

[7] Lombardini, F., Gini, F., and Matteucci, P. (2001), Application of array processing techniques to multibaseline InSAR for layover solution, In *Proceedings of the 2001 IEEE Radar Conference, 2001*, pp. 210–215.

[8] Zhu, X. X. (2008), Spectral Estimation for Synthetic Aperture Radar Tomography, Masters, Technische Universität München, Earth Oriented Space Science and Technology – ESPACE.

[9] Fornaro, G., Serafino, F., and Soldovieri, F. (2003), Three-dimensional focusing with multipass SAR data, *IEEE Transactions on Geoscience and Remote Sensing*, 41(3), 507–517.

[10] Budillon, A., Evangelista, A., and Schirinzi, G. (2009), SAR tomography from sparse samples, In *Geoscience and Remote Sensing Symposium,2009 IEEE International, IGARSS 2009*, Vol. 4, pp. IV–865–IV–868.

[11] Budillon, A., Evangelista, A., and Schirinzi, G. (2010), SAR tomographic focusing by Compressive Sampling: Experiments on real data, In *Geoscience and Remote Sensing Symposium (IGARSS), 2010 IEEE International*, pp. 3785–3788.

[12] Budillon, A., Evangelista, A., and Schirinzi, G. (2011), Three-Dimensional SAR Focusing From Multipass Signals Using Compressive Sampling, *IEEE Transactions on Geoscience and Remote Sensing*, 49(1), 488–499.

[13] Budillon, A., and Schirinzi, G. (2011), Artifact reduction in SAR Compressive Sampling tomography, In *Geoscience and Remote Sensing Symposium (IGARSS), 2011 IEEE International*, pp. 2700–2703.

[14] Zhu, X. X., and Bamler, R. (2011), Sparse reconstrcution techniques for SAR tomography, In *2011 17th International Conference on Digital Signal Processing (DSP)*, pp. 1–8.

[15] Zhu, X. X., and Bamler, R. (2010), Very High Resolution Spaceborne SAR Tomography in Urban Environment, *IEEE Transactions on Geoscience and Remote Sensing*, 48(12), 4296–4308.

[16] Carrara, W. G., Majewski, R. M., and Goodman, R. S. (1995), Spotlight Synthetic Aperture Radar: Signal Processing Algorithms, Boston: Artech House.

[17] Tebaldini, S., and Rocca, F. (2009), On the impact of propagation disturbances on SAR Tomography: Analysis and compensation, In *2009 IEEE Radar Conference*, pp. 1–6.

[18] Tebaldini, S., and Monti Guarnieri, A. (2010), On the Role of Phase Stability in SAR Multibaseline Applications, *IEEE Transactions on Geoscience and Remote Sensing*, 48(7), 2953–2966.

[19] Candès, E. J., Romberg, J. K., and Tao, T. (2006), Stable signal recovery from incomplete and inaccurate measurements, *Communications on Pure and Applied Mathematics*, 59(8), 1207–1223.

[20] Candes, E., Romberg, J., and Tao, T. (2006), Robust uncertainty principles: exact signal reconstruction from highly incomplete frequency information, *Information Theory, IEEE Transactions on*, 52(2), 489–509.

[21] Candes, E., and Tao, T. (2006), Near-Optimal Signal Recovery From Random Projections: Universal Encoding Strategies?, *Information Theory, IEEE Transactions on*, 52(12), 5406–5425.

[22] Baraniuk, R. (2007), Compressive Sensing, *IEEE Signal Processing Magazine*, 24(4), 118–121.

[23] Candes, E., and Wakin, M. (2008), An Introduction To Compressive Sampling, *Signal Processing Magazine, IEEE*, 25(2), 21–30.

[24] Chen, P.-H., and Dowman, I. (2001), A weighted least squares solution for space intersection of spaceborne stereo SAR data, *IEEE Transactions on Geoscience and Remote Sensing*, 39(2), 233–240.

[25] Parker, J. T., Ferrara, M. A., and Potter, L. C. (2012), Radar Applications of Sparse Reconstruction and Compressed Sensing, In *Principles of Modern Radar: Advanced Techniques*, Scitech Publishing Inc.

[26] Michael R. Osborne, Brett Presnell, and Berwin A. Turlach (2000), On the LASSO and its Dual, *Journal of Computational and Graphical Statistics*, 9(2), 319–337.

[27] van den Berg, E., and Friedlander, M. P. (2009), Probing the Pareto Frontier for Basis Pursuit Solutions, *SIAM Journal on Scientific Computing*, 31(2), 890–912.

[28] Becker, S., Bobin, J., and Candès, E. J. (2011), NESTA: A Fast and Accurate First-Order Method for Sparse Recovery, *SIAM Journal on Imaging Sciences*, 4(1), 1–39.

[29] Figueiredo, M., Nowak, R., and Wright, S. (2007), Gradient Projection for Sparse Reconstruction: Application to Compressed Sensing and Other Inverse Problems, *Selected Topics in Signal Processing, IEEE Journal of*, 1(4), 586 –597.

[30] Zhu, X. X., Wang, Y., and Bamler, R. (2012), Integration of tomographic SAR inversion and PSI for operational use, In *9th European Conference on Synthetic Aperture Radar, 2012. EUSAR*, pp. 151–154.

[31] Hale, E. T., Yin, W., and Zhang, Y. (2010), Fixed-Point Continuation Applied to Compressed Sensing: Implementation and Numerical Experiments, *Journal of Computational Mathematics*.

[32] Candès, E. (2006), Compressive Sampling, In *Proceedings of the International Congress of Mathematicians*, Vol. 3, pp. 1433–1452, Madrid, Spain.

[33] Candès, E., and Romberg, J. (2007), Sparsity and incoherence in compressive sampling, *Inverse Problems*, 23(3), 969–985.

[34] Foucart, S., and Rauhut, H. (2013), A Mathematical Introduction to Compressive Sensing, 2013 edition ed, Birkhäuser.

[35] Elad, M. (2010), Sparse and Redundant Representations: From Theory to Applications in Signal and Image Processing, 2010 edition ed, New York: Springer.

[36] Ghaoui, L. E., and Lebret, H. (1997), Robust Solutions to Least-Squares Problems with Uncertain Data, *SIAM J. Matrix Anal. Appl.*, 18(4), 1035–1064.

[37] Markovsky, I., and Van Huffel, S. (2007), Overview of total least-squares methods, *Signal Processing*, 87(10), 2283–2302.

[38] Herman, M., and T. Strohmer (2010), General Deviants: An Analysis of Perturbations in Compressed Sensing, *IEEE Journal of Selected Topics in Signal Processing*, 4(2), 342–349.

[39] Chi, Y., Pezeshki, A., Scharf, L., and Calderbank, R. (2010), Sensitivity to basis mismatch in compressed sensing, In *2010 IEEE International Conference on Acoustics Speech and Signal Processing (ICASSP)*, pp. 3930–3933.

[40] Chi, Y., Scharf, L., Pezeshki, A., and Calderbank, A. (2011), Sensitivity to Basis Mismatch in Compressed Sensing, *Signal Processing, IEEE Transactions on*, 59(5), 2182–2195.

[41] Zhu, W., Wang, Y., Yao, Y., Chang, J., Graber, H. L., and Barbour, R. L. (1997), Iterative total least-squares image reconstruction algorithm for optical tomography by the conjugate gradient method, *Journal of the Optical Society of America A*, 14(4), 799–807.

[42] Zhu, X. X., and Bamler, R. (2011), Within the resolution cell: Super-resolution in tomographic SAR imaging, In *Geoscience and Remote Sensing Symposium (IGARSS), 2011 IEEE International*, pp. 2401–2404.

[43] Han, X., Zhang, H., and Meng, H. (2011), TLS-FOCUSS for sparse recovery with perturbed dictionary, In *2011 IEEE International Conference on Acoustics, Speech and Signal Processing (ICASSP)*, pp. 3952–3955.

[44] Beck, A., and Teboulle, M. (2009), A fast Iterative Shrinkage-Thresholding Algorithm with application to wavelet-based image deblurring, In *IEEE International Conference on Acoustics, Speech and Signal Processing, 2009. ICASSP 2009*, pp. 693–696.

[45] Swingler, D. (1993), Frequency Estimation for Closely Spaced Sinsoids: Simple Approximations to the Cramer-Rao Lower Bound, *IEEE Transactions on Signal Processing*, 41(1), 489–495.

[46] Rife, D., and Boorstyn, R. (1976), Multiple tone parameter estimation from discrete-time observations, *Bell System Technical Journal, The*, 55(9), 1389–1410.

[47] Varshney, K., Cetin, M., Fisher, J., and Willsky, A. (2008), Sparse Representation in Structured Dictionaries With Application to Synthetic Aperture Radar, *IEEE Transactions on Signal Processing*, 56(8), 3548–3561.

[48] Hu, N., Ye, Z., Xu, D., and Cao, S. (2012), A sparse recovery algorithm for DOA estimation using weighted subspace fitting, *Signal Processing*, 92(10), 2566–2570.

[49] Angeliki Xenaki, Peter Gerstoft, and Efren Fernandez-Grande (2015), Sparse DOA estimation with polynomial rooting, In *3rd International Workshop on Compressed Sensing Theory and its Applications to Radar, Sonar, and Remote Sensing*, Pisa, Italy.

[50] Panahi, A., and Viberg, M. (2014), Gridless compressive sensing, In *2014 IEEE International Conference on Acoustics, Speech and Signal Processing (ICASSP)*, pp. 3385–3389.

[51] Stoica, P., Tangy, G., Yang, Z., and Zachariah, D. (2014), Gridless compressive-sensing methods for frequency estimation: Points of tangency and links to basics, In *Signal Processing Conference (EUSIPCO), 2014 Proceedings of the 22nd European*, pp. 1831–1835.

This page intentionally left blank.

Annex A: Derivation of range approximation

We start by the Range Equation (6) and factor out $\sqrt{R_0^2+u^2}$, to give:

$$\begin{aligned} R(u) &= \sqrt{R_0^2+(u-s)^2} \\ &= \sqrt{R_0^2+u^2}\sqrt{1-\frac{2us-s^2}{R_0^2+u^2}}. \end{aligned} \tag{A.1}$$

We now perform a Taylor series expansion for the second square root factor w.r.t. the variable s around the point $s=0$. Evaluating the square root at $s=0$ gives:

$$\sqrt{1-\frac{2us-s^2}{R_0^2+u^2}}\bigg|_{s=0} = 1. \tag{A.2}$$

Taking the partial derivative w.r.t. to s_q and evaluating it at the point $s_q=0$ gives:

$$\begin{aligned} \frac{\partial}{\partial s_q}\sqrt{1-\frac{2us-s^2}{R_0^2+u^2}}\bigg|_{s=0} &= \frac{1}{2}\left(1-\frac{2us-s^2}{R_0^2+u^2}\right)^{-\frac{1}{2}}\cdot\left(-\frac{2u-2s}{R_0^2+u^2}\right)\bigg|_{s=0} \\ &= -\frac{u}{R_0^2+u^2}. \end{aligned} \tag{A.3}$$

The resulting Taylor series is given by:

$$\sqrt{1-\frac{2us-s^2}{R_0^2+u^2}} \approx 1-\frac{us}{R_0^2+u^2}. \tag{A.4}$$

Substituting this back into (A.1) gives:

$$\begin{aligned} R(u) &\approx \sqrt{R_0^2+u^2}\left(1-\frac{us}{R_0^2+u^2}\right) \\ &= \sqrt{R_0^2+u^2}-\frac{us}{\sqrt{R_0^2+u^2}}. \end{aligned} \tag{A.5}$$

Now assuming that $u \ll R_0$ then a further approximation is gives:

$$R(u) = \sqrt{R_0^2+u^2}-\frac{us}{R_0}. \tag{A.6}$$

This page intentionally left blank.

Annex B: FISTA algorithm

For a given value of λ we wish to solve the following problem:

$$\min_{\boldsymbol{x}} \|\boldsymbol{A}\boldsymbol{x} - \boldsymbol{y}\|_2^2 + \lambda \|\boldsymbol{x}\|_1 . \tag{B.1}$$

We first define a soft thresholding operating on a scalar as:

$$\eta_s(x, \alpha) = \begin{cases} \left(\frac{|x|-\alpha}{|x|}\right) x, & \text{if } |x| \geq \alpha \\ 0, & \text{otherwise.} \end{cases} \tag{B.2}$$

In other words, the amplitude of the scalar is reduced by the value α or set to zero if the amplitude is already equal to or less than α. When operating on a vector the function $\eta_s(\cdot\,, \alpha)$ operates component-wise. The FISTA algorithm is then given by:

$$\begin{aligned} &\boldsymbol{z}^1 = \boldsymbol{x}^0 = \boldsymbol{0} \\ &t^1 = 0 \\ &\boldsymbol{x}^k = \eta_s\left(\boldsymbol{z}^k - \frac{2}{P}\boldsymbol{A}^H(\boldsymbol{A}\boldsymbol{z}^k - \boldsymbol{y}), \frac{\lambda}{P}\right) \\ &t^{k+1} = \frac{1 + \sqrt{1 + 4(t^k)^2}}{2} \\ &\boldsymbol{z}^{k+1} = \boldsymbol{x}^k + \frac{t^k - 1}{t^{k+1}}(\boldsymbol{x}^k - \boldsymbol{x}^{k-1}), \end{aligned}$$

where P is twice the largest eigenvalue of $\boldsymbol{A}^H\boldsymbol{A}$ and the superscripts k and $k+1$ denote time iterations.

This page intentionally left blank.

Annex C: List of Symbols / Acronyms

BP	Basis Pursuit
BPDN	Basis Pursuit De-Noising
CRLB	Cramer Rao Lower Bound
CS	Compressive Sensing
dB	Decibels
FISTA	Fast Iterative Shrinkage and Thresholding Algorithm
InSAR	Interferrometric Synthetic Aperture Radar
LASSO	Least Absolute Shrinkage and Selection Operator
RCM	RADARSAT Constellation Mission
RIP	Restricted Isometry Property
SAR	Synthetic Aperture Radar
SNR	Signal to Noise Ratio
STK	Systems Toolkit
SVD	Singular Value Decomposition

This page intentionally left blank.

DOCUMENT CONTROL DATA

(Security markings for the title, abstract and indexing annotation must be entered when the document is Classified or Protected.)

1. ORIGINATOR (The name and address of the organization preparing the document. Organizations for whom the document was prepared, e.g. Centre sponsoring a contractor's report, or tasking agency, are entered in section 8.)

DRDC – Ottawa Research Centre
3701 Carling Avenue, Ottawa ON K1A 0Z4, Canada

2a. SECURITY MARKING (Overall security marking of the document, including supplemental markings if applicable.)

UNCLASSIFIED

2b. CONTROLLED GOODS

(NON-CONTROLLED GOODS)
DMC A
REVIEW: GCEC DECEMBER 2012

3. TITLE (The complete document title as indicated on the title page. Its classification should be indicated by the appropriate abbreviation (S, C or U) in parentheses after the title.)

Study of Compressive Sensing for Tomographic Processing in Satellite (SAR) Systems

4. AUTHORS (Last name, followed by initials – ranks, titles, etc. not to be used.)

Kirkland, D.

5. DATE OF PUBLICATION (Month and year of publication of document.)	6a. NO. OF PAGES (Total containing information. Include Annexes, Appendices, etc.)	6b. NO. OF REFS (Total cited in document.)
September 2016	84	51

7. DESCRIPTIVE NOTES (The category of the document, e.g. technical report, technical note or memorandum. If appropriate, enter the type of report, e.g. interim, progress, summary, annual or final. Give the inclusive dates when a specific reporting period is covered.)

Scientific Report

8. SPONSORING ACTIVITY (The name of the department project office or laboratory sponsoring the research and development – include address.)

DRDC – Ottawa Research Centre
3701 Carling Avenue, Ottawa ON K1A 0Z4, Canada

9a. PROJECT OR GRANT NO. (If appropriate, the applicable research and development project or grant number under which the document was written. Please specify whether project or grant.)	9b. CONTRACT NO. (If appropriate, the applicable number under which the document was written.)
05EA	

10a. ORIGINATOR'S DOCUMENT NUMBER (The official document number by which the document is identified by the originating activity. This number must be unique to this document.)	10b. OTHER DOCUMENT NO(s). (Any other numbers which may be assigned this document either by the originator or by the sponsor.)
DRDC-RDDC-2016-R173	

11. DOCUMENT AVAILABILITY (Any limitations on further dissemination of the document, other than those imposed by security classification.)

Unlimited

12. DOCUMENT ANNOUNCEMENT (Any limitation to the bibliographic announcement of this document. This will normally correspond to the Document Availability (11). However, where further distribution (beyond the audience specified in (11)) is possible, a wider announcement audience may be selected.)

Unlimited

13. ABSTRACT (A brief and factual summary of the document. It may also appear elsewhere in the body of the document itself. It is highly desirable that the abstract of classified documents be unclassified. Each paragraph of the abstract shall begin with an indication of the security classification of the information in the paragraph (unless the document itself is unclassified) represented as (S), (C), or (U). It is not necessary to include here abstracts in both official languages unless the text is bilingual.)

Tomographic processing involves coherent processing of multiple passes of Synthetic Aperture Radar (SAR) imagery to provide elevation discrimination in a SAR range/azimuth pixel. This report investigates the use of C-band satellites such as RADARSAT-2 or the RADARSAT Constellation Mission (RCM) for tomographic processing. This report uses a Compressive Sensing (CS) approach to accomplish the tomographic processing. Four different satellite geometries are simulated to provide a range of operating environments. For each of the geometries the performance against single target and two target scenarios is measured at various Signal to Noise ratios (SNRs) using simulated data. This report also includes theoretical analysis on the resolution and the Cramer-Rao Lower Bounds (CRLB) on the deviation of elevation estimates.

14. KEYWORDS, DESCRIPTORS or IDENTIFIERS (Technically meaningful terms or short phrases that characterize a document and could be helpful in cataloguing the document. They should be selected so that no security classification is required. Identifiers, such as equipment model designation, trade name, military project code name, geographic location may also be included. If possible keywords should be selected from a published thesaurus. e.g. Thesaurus of Engineering and Scientific Terms (TEST) and that thesaurus identified. If it is not possible to select indexing terms which are Unclassified, the classification of each should be indicated as with the title.)

SAR Imaging
Compressive Sensing
Tomography

DRDC | RDDC

SCIENCE, TECHNOLOGY AND KNOWLEDGE FOR CANADA'S DEFENCE AND SECURITY | SCIENCE, TECHNOLOGIE ET SAVOIR POUR LA DÉFENSE ET LA SÉCURITÉ DU CANADA

www.drdc-rddc.gc.ca